Driving mechanisms of organic carbon burial in the Early Cretaceous South Atlantic Cape Basin (DSDP Site 361)

Wolf Dummann[1,a], Sebastian Steinig[2,b], Peter Hofmann[1], Matthias Lenz[1], Stephanie Kusch[1], Sascha Flögel[2], Jens O. Herrle[3], Christian Hallmann[4,5], Janet Rethemeyer[1], Haino U. Kasper[1], Thomas Wagner[6]

[1]Institute of Geology and Mineralogy, University of Cologne, Cologne, D-50674, Germany
[2]GEOMAR Helmholtz Centre for Ocean Research Kiel, Kiel, D-24148 Kiel, Germany
[3]Institute of Geosciences, Goethe-University Frankfurt, Frankfurt am Main, D-60438, Germany
[4]Max Planck Institute for Biogeochemistry, Jena, D-07745, Germany
[5]MARUM, University of Bremen, Bremen, D-28359, Germany
[6]Lyell Centre, School of Energy, Geoscience, Infrastructure and Society, Heriot-Watt University, Edinburgh, EH14 4AS, UK
[a]now at: Institute of Geosciences, Goethe-University Frankfurt, Frankfurt am Main, D-60438, Germany
[b]now at: School of Geographical Sciences, University of Bristol, Bristol, BS8 1SS, UK

Correspondence to: Wolf Dummann (wdummann@uni-koeln.de)

Abstract. Extensive black shale deposits formed in the Early Cretaceous South Atlantic, supporting the notion that this emerging ocean basin was a globally important site of organic carbon burial. The magnitude of organic carbon burial in marine basins is known to be controlled by various tectonic, oceanographic, hydrological, and climatic processes acting on different temporal and spatial scales, the nature and relative importance of which are poorly understood for the young South Atlantic. Here we present new bulk and molecular geochemical data from an Aptian–Albian sediment record recovered from the deep Cape Basin at Deep Sea Drilling Project (DSDP) Site 361, which we combine with general circulation model results to identify driving mechanisms of organic carbon burial. A multi-million year decrease (i.e. Early Aptian–Albian) in organic carbon burial, reflected in a lithological succession of black shale, gray shale, and red beds, was caused by increasing bottom water oxygenation due to abating hydrographic restriction via South Atlantic-Southern Ocean gateways. These results emphasize basin evolution and ocean gateway development as a decisive primary control on enhanced organic carbon preservation in the Cape Basin at geological time scales (>1 Myr). The Early Aptian black shale sequence comprises alternations of shales with high (>6%) and relatively low (~3.5%) organic carbon content of marine sources, the former being deposited during the global Oceanic Anoxic Event (OAE) 1a, as well as during repetitive intervals before and after OAE 1a. In all cases, these short-term intervals of enhanced organic carbon burial coincided with strong influxes of sediments derived from the proximal African continent, indicating closely coupled climate–land–ocean interactions. Supported by our model results, we show that fluctuations in weathering-derived nutrient input from the southern African continent, linked to changes in orbitally driven humidity/aridity, were the underlying drivers of repetitive episodes of enhanced organic carbon burial in the deep Cape Basin. These results suggest that deep marine environments of emerging ocean basins responded sensitively and directly to short-term fluctuations in riverine nutrient fluxes. We explain this relationship by the lack of wide and mature continental shelf seas that could have acted as a barrier or filter for nutrient transfer from the continent into the deep ocean.

1   Introduction

35   The Early Cretaceous epoch (~145–100.5 Ma) has long been a focus of interest for geologists and the petroleum industry due to the widespread occurrence of marine black shales (i.e. organic carbon rich, fine-grained sediments), which were preferentially deposited in emerging ocean basins that developed in the wake of the breakup of Pangaea (Stein et al., 1986; Zimmerman et al., 1987). Within these basins, organic carbon (OC) burial was controlled by a complex interplay of productivity, preservation, and dilution (Pedersen and Calvert, 1990; Tyson, 2005; Arthur and Sageman, 1994; Bralower and

40   Thierstein, 1984), which was affected by multiple processes acting on different time scales. On a multi-million year (geological) time scale, OC burial was controlled by tectonic processes modifying basin geometry, marine gateway evolution, and ocean circulation (Donnadieu et al., 2016; Dummann et al., 2020; Arthur and Natland, 1979; Wagner and Pletsch, 1999), while shorter term (e.g. orbitally driven) changes in oceanic and atmospheric circulation triggered pronounced fluctuations in the magnitude of OC burial on time scales of ten to hundred thousand years (Beckmann et al., 2005; Behrooz et al., 2018;

45   Hofmann and Wagner, 2011; Wagner et al., 2013; Kolonic et al., 2005; Herrle et al., 2003). During brief episodes ≤1 Myr, marine black shales were deposited regionally to globally and accompanied by intense perturbations in ocean chemistry and ecology (Jenkyns, 2010; Weissert et al., 1998; Erba, 1994). These carbon–climate perturbation events are described as Oceanic Anoxic Events (OAEs; Schlanger and Jenkyns, 1976). OAE 1a, one of the most severe OAEs (Jenkyns, 2010 and references therein), occurred during the Early Aptian (Coccioni et al., 1992) and was marked by a distinct negative stable carbon isotope

50   excursion at its onset (Menegatti et al., 1998), evidence for rapid warming (O'Brien et al., 2017 and references therein), and elevated atmospheric CO_2 concentrations (Naafs et al., 2016).

During the Early Aptian, at the time of OAE 1a, the emerging South Atlantic Ocean consisted of two main rift basins that progressively opened from South to North (Pérez-Díaz and Eagles, 2017) and which were separated from each other by the volcanic Walvis Ridge (Figure 1). Each of the two sub-basins acted as a major depocenter for OC-rich sediments (Zimmerman

55   et al., 1987; Arthur and Natland, 1979; Macdonald et al., 2003) with exceptionally high OC burial rates in the Early Cretaceous. Biogeochemical modeling indicates that excess OC burial in the South Atlantic basin may have accounted for around 16% of global OC burial during the Aptian in an area that covered only around 1% of the total global ocean (McAnena et al., 2013). Data from Deep Sea Drilling Project (DSDP) Site 364, located at a paleo-latitude of 25° S and an estimated paleo-water depth of ~300–400 m (Zimmerman et al., 1987) in the Angola Basin (Figure 1), suggest that enhanced OC deposition occurred north

60   of the Walvis Ridge during the Early to early Late Aptian, sustained by the restricted basin geometry and the continuous supply of nutrients from surrounding continents (Arthur and Natland, 1979; Behrooz et al., 2018; Naafs and Pancost, 2014). In line with previous studies (e.g. Beckmann et al., 2005), a recent study by Behrooz et al. (2018) indicates that marine OC burial dynamics at Site 364 were tightly coupled to orbitally driven continental hydrology and run-off variability beneath the ascending, tropical limb of the atmospheric Hadley Cell (the Intertropical Convergence Zone; ITCZ). Near-shore sediment

65   records located along continental margins, such as Site 364, often show particularly pronounced cycles of variable OC quantity and quality, as this is where hydrological changes on the continent are most directly translated into marine sediments, while

less pronounced cycles at sites further offshore reflect an attenuation of the signal with increasing water depth and distance from the continent (Wagner et al., 2013).

Our study investigates the driving mechanisms of marine OC burial in the deep Cape Basin (Figure 1), south of the Walvis Ridge, and their connections to mid-latitude atmospheric circulation and continental hydrology, which have been studied less extensively. We provide new inorganic and organic (bulk and molecular) geochemical data from DSDP Site 361, located at a paleo-latitude of ~45° S and a paleo-water depth of 2–2.5 km (Figure 1; Melguen, 1978; Thiede and Van Andel, 1977; Van Andel et al., 1977), where an extensive Aptian black shale sequence was recovered (The Shipboard Scientific Party, 1978), including OAE 1a (Dummann et al., 2020). These black shales show repetitive alternations of OC-rich and (relatively) OC-poor sediments (Dummann et al., 2020), indicating highly dynamic depositional conditions on a time scale of <1 Myr. We combine our new proxy data with general circulation model (GCM) data to provide insights into the nature and pacing of cyclic fluctuations in atmospheric circulation and continental hydrology at mid-latitudes during the Early Cretaceous to evaluate its importance for open marine OC burial dynamics in the deep Cape Basin.

1.1 Geological setting and stratigraphy of DSDP Site 361

1.1.1 Lithostratigraphy

Site 361 was drilled on the lower continental rise of South Africa (35°03.97' S, 15°26.91' E) at a modern water depth of 4,549 m (The Shipboard Scientific Party, 1978). A total of 390 m of Early Cretaceous sediments were penetrated with an average core recovery of ~32% (Figure 2a). The shipboard scientific party of DSDP Leg 40 divided the Early Cretaceous sediment sequence into two lithostratigraphic units (The Shipboard Scientific Party, 1978). The lower unit (cores 28–48; Figure 2a) is of Early Aptian age and was deposited in a deep proximal fan to fan-valley environment (Kagami, 1978; Natland, 1978). Shale intervals occur scattered throughout the Early Aptian sequence and are intercalated with sand- and siltstone beds, which account for ~55% of the recovered sediments (Figure 2a). These coarse-grained beds have been interpreted as turbidites, dense traction or debris flows, and potentially bed loads (Natland, 1978). Intercalated shales are mostly fissile, partly laminated, and frequently lack bioturbation, indicating deposition under conditions of reduced bottom water oxygenation (Natland, 1978; Arthur and Natland, 1979; Thiede and Van Andel, 1977). Sedimentological evidence suggests that shales are partly of hemipelagic and turbiditic origin. The former are up to several meters thick and frequently comprise thin alternations of nannofossil layers and mudstone intervals, indicating fluctuating deposition under tranquil conditions (Natland, 1978). The latter are associated with sandstone and sandy mudstone beds and presumably represent fine-grained turbiditic material, which settled out of suspension (Kagami, 1978).

The overlying lithostratigraphic unit (cores 26–27; Figure 2a) consists of Late Aptian gray shales and Albian red beds, in which cross-laminated siltstone beds and burrowing structures become abundant (Natland, 1978; The Shipboard Scientific Party, 1978), reflecting a strengthening of deep water circulation and ventilation, respectively (Arthur and Natland, 1979). Sandstone beds become less frequent, which has been linked to subsidence and/or erosion of sediment source regions along the SW

African margin (Natland, 1978). This profound change in the sedimentary environment of the Cape Basin resulted from an intensified deep water mass exchange with the adjacent Southern Ocean basin (Arthur and Natland, 1979) due to the progressive opening of two gateways, namely the shallow Falkland Plateau Gateway and deep Georgia Basin Gateway (Dummann et al., 2020).

In the present study, we divide the sedimentary sequence into three lithostratigraphic units, which largely conform with the units defined by the shipboard scientific party: (1) a black shale unit present in cores 48–28 (Figure 2a), (2) a gray shale unit in core 27, and red beds in core 26. Gray shales and red beds are subdivided into two lithostratigraphic units based on their distinct color and TOC content (Figure 2c), as proposed by Dummann et al. (2020).

1.1.2 Biostratigraphy and carbon isotope stratigraphy

Age constraints for Early Cretaceous sediments at Site 361 are mainly based on calcareous nannofossil biostratigraphy, originally defined by Proto Decima et al. (1978) and recently updated by Dummann et al. (2020), indicating an Early Aptian–Albian age for the investigated sediment sequence (Figure 2a). Supported by biostratigraphy (i.e. first occurrence of *Eprolithus floralis* at ~1065 mbsf), Dummann et al. (2020) further identified OAE 1a in the Early Aptian black shale unit between 1089 and 1050 mbsf, based on its characteristic carbon isotope excursions (Figure 2b; Menegatti et al., 1998).

2 Materials and methods

2.1 Sampling strategy

Sampling at Site 361 primarily targeted hemipelagic shale intervals, while turbiditic coarse-grained sediments and associated shale intervals (i.e. cm–dm thick shale intervals, which lie on top and in-between sandstone beds) were omitted. The geochemistry of turbiditic sediments has, however, been described in previous studies (e.g. Jacquin and De Graciansky, 1988; Natland, 1978; Kagami, 1978). These studies indicate that turbidites were derived from granitic weathering source regions along the proximal SW African coast (Natland, 1978). TOC contents of sandstones cover a similar range as hemipelagic shales (Jacquin and De Graciansky, 1988) with a strong dominance of terrigenous OC, including preserved coal particles and wood fragments (Jacquin and De Graciansky, 1988; Raynaud and Robert, 1978). This OC was probably entrained by turbidites and transported from the shelf to the deeper basin. To ensure homogenous grain-size characteristics among all investigated samples, the samples were screened using geochemical grain-size proxies (i.e. Si/Al and Zr/Al ratios; e.g. Croudace and Rothwell, 2015 and references therein) and compared to a number of reference samples (*n*=8) taken from turbiditic sandstones (Figure 3a).

2.2 Analytical methods

2.2.1 Major and trace element analysis by XRF

Major (Al, Si, K, Ti) and trace element (Zr, Ni, Cu, V, Zn) concentrations were determined on 131 shale samples and 8 sandstones using an Itrax x-ray fluorescence (XRF) Core Scanner (Cox Analytical Systems, Sweden) equipped with a Cr-tube. Dried and ground samples were pressed into plastic cubes, which were aligned under the core scanner. Analyses were performed at a resolution of 1 mm and an integration time of 60 s per measurement, yielding nine to twelve individual measurements per sample, which were averaged over each sample. Absolute element concentrations were quantified by calibration against reference samples of known elemental composition, which were measured alongside the samples (for details see Supplement S1).

2.2.2 Trace element analysis by ICP-MS

In addition to XRF analysis, 15 black shale samples covering a range of TOC values from 2.5–15.7% were investigated for their immobile trace element (Th, Sc, Zr) and rare earth element (REE) composition. Analyses were conducted using a SCIEX ELAN 6100 inductively coupled plasma mass spectrometer (ICP-MS; Perkin Elmar, USA) following total acid digestion. Aliquots of dried and ground samples were combusted at 550 °C for 4 h to remove OC and subsequently decomposed in a 6 AM pressure digestion system (PDS6, Loftfields Analytical Solutions, Germany), following published protocols (Dulski, 2001). Acids used for digestion were HF (40%, suprapure, Merck, Germany), HNO_3 (65%, suprapure, Merck, Germany), $HClO_4$ (70%, ultrapure, VWR, USA), and HCl (30%, suprapure, Merck, Germany). Quantification was conducted using two external multi-element standard solutions (1 ng^{-1}, 10 ng^{-1}) and a matrix solution. An internal Ru-Re standard was analyzed alongside the samples to monitor instrumental drift. Two certified reference materials (CRM) JA-2 (Dulski, 2001) and GA (Govindaraju, 1994) were used to monitor precision and accuracy. All standards reproduced within ± 3%.

2.2.3 Lipid biomarker analysis

Aliquots from 71 samples (1–8 grams) were extracted with methanol (Merck SupraSolv®, Germany; 30 mL), methanol–dichloromethane (1:1, v:v; 30 mL), and dichloromethane (Merck SupraSolv®, Germany; 30 mL) for 10 minutes each in an ultrasonic bath. The extracts were combined in a separatory funnel and mixed with ultrapure water to remove methanol. The dichloromethane fraction was decanted and dried under mild vacuum (40 ºC, 800 mbar) using a rotary evaporator. Acid-activated copper turnings were added to the extracts to remove elemental sulfur. The samples were saponified using a 0.5 molar potassium hydroxide solution (methanol–water 9:1, v:v). Neutral lipids were extracted from the saponification solution with hexane (Merck SupraSolv®, Germany) and partitioned into three polarity fractions (aliphatic hydrocarbons, aromatic hydrocarbons, and heteroatomic NSO-compounds) over a self-packed silica column (500 mg, 0.063–0.200 mm, 70–230 mesh, Merck, Germany; deactivated with 1% ultrapure water) using hexane, hexane–dichloromethane (2:1, v:v), and dichloromethane–methanol (1:1, v:v), respectively. To reduce interferences during mass spectrometric analysis, the aliphatic

fraction was further separated into saturated and unsaturated compounds using silver-ion chromatography (10% AgNO$_3$-coated silica gel, Sigma-Aldrich, USA), which were eluted with hexane and ethyl acetate (Merck SupraSolv®, Germany), respectively. Deuterated internal standards (i.e. d_{50}-tetracosane and d_4-cholestane) were used for quantification and added to the saturated aliphatic fraction prior to analysis.

160   The saturated aliphatic fractions were analyzed using coupled gas chromatography-mass spectrometry (GC-MS) and GC-MS/MS. The distribution of acyclic hydrocarbons (i.e. *n*-alkanes, acyclic isoprenoids) was analyzed using an Agilent 6890N GC coupled to an Agilent 5975 MSD operated in selected ion monitoring (SIM) mode scanning for *m/z* 85 ([C$_6$H$_{13}$]$^+$) and *m/z* 98 ([C$_6$D$_{13}$]$^+$) fragments. Samples were injected onto a DB5-MS column (50 m, 0.2 mm, 0.25 µm) using a split/splitless injector operated in splitless mode and heated from 70 °C to 250 °C. Helium was used as carrier gas at a constant flow rate of 1.3 mL

165   min^{-1}. The GC temperature was held at 40 °C for 2 min, increased to 140 °C at 10 °C min^{-1} and to 320 °C at 5 °C min^{-1}. The final temperature was held for 22 min. Ionization was achieved by electron impact (EI) at 70 eV and 230 ºC. Reproducibility was monitored using an authentic *n*-alkane standard solution and was better than 1%.

Sterane and hopane distributions were analyzed using an Agilent 7890B GC coupled to an Agilent 7000C EI-TQ-MS operated in multiple reaction monitoring (MRM) mode. Samples were injected onto a HP5-MS column (50 m, 0.25 mm, 0.25 µm) using

170   a split/splitless injector operated in splitless mode at 290 °C. Helium was used as carrier gas at a constant flow rate of 1.2 mL min^{-1}. The initial GC temperature was held at 60 °C for 2 min, then increased to 140 °C at 10 °C min^{-1} and to 320 °C at 4 °C min^{-1}, which was held for 15 min. Ionization was achieved by EI at 70 eV and 300 ºC. Argon was used as a collision gas at a collision energy of 10 V. Reproducibility was monitored using an in-house standard containing all targeted compounds at similar concentration levels. The reproducibility of measurements varied between different compounds and was mostly better

175   than 5%, but always better than 10% for all reported biomarker ratios.

2.3   General circulation modeling

Model simulations were carried out with the Kiel Climate Model (KCM; Park et al., 2009). The KCM uses the ECHAM5 spectral atmospheric model with a horizontal resolution of ~2.8° (T42) on 19 vertical levels (Roeckner et al., 2003) coupled to the ocean–sea ice component NEMO (Madec, 2008) on a tripolar grid with a horizontal resolution of 2° (ORCA2) and 31

180   vertical levels. The meridional ocean resolution gradually increases to 0.5° towards the equator. Modifications to the model for the Early Cretaceous configuration are described in Dummann et al. (2020). We slightly modified the bathymetry of the area north of the Walvis Ridge (~30° S) by replacing the Early Albian paleo-bathymetry used in Dummann et al. (2020) with the Early Aptian boundary conditions of Sewall et al. (2007) to account for the reduced northward extent of the Angola Basin during the Aptian (Supplementary Figure 1 in Supplement S4).

185   Two 3,000 year-long simulations with atmospheric *p*CO$_2$ levels of 600 ppm and 1200 ppm were performed to reflect published range of stomata-based *p*CO$_2$ reconstructions for the Aptian–Albian (Jing and Bainian, 2018) and enhanced *p*CO$_2$ levels during OAE 1a (Naafs et al., 2016), respectively. Even though peak *p*CO$_2$ concentrations during the hyperthermal phase of OAE 1a may have been even higher (Naafs et al., 2016), Steinig et al. (2020) showed that the KCM is capable of simulating upper

ocean temperatures at a pCO$_2$ of 1200 ppm, which are broadly consistent with the lower end of proxy reconstructions for OAE
190 1a. This model-data congruence can be achieved by assuming a regional warm bias in the Early Cretaceous TEX$_{86}$ record in
the young Atlantic Ocean. We are therefore confident that our 1200 ppm pCO$_2$ model represents an OAE 1a-like climate state
reasonably well, while the 600 ppm simulation rather reflects lower Early Cretaceous background pCO$_2$ levels (Jing and
Bainian, 2018). Results were averaged over the last 100 model years, when the model reached a quasi-steady state with a
globally depth-integrated temperature drift over 1,000 model years of below 0.2 °C (Supplementary Figure 2 in Supplement
195 S4).

We further performed orbital sensitivity experiments at 600 and 1200 ppm pCO$_2$ to assess the influence of cyclic fluctuations
in solar insolation on continental hydrology. Numerical solutions for orbital parameters beyond ~50 Ma become highly
uncertain (Laskar et al., 2011). We therefore followed the method of Crowley et al. (1993) and defined two end-member
configurations representing maxima and minima in summer insolation, implementing Pleistocene ranges for eccentricity,
200 obliquity, and precession (Berger, 1978). Both simulations with low and high pCO$_2$ concentrations used a constant eccentricity
of 0.06 with varying obliquity and precession to create a "warm summer orbit" (24.5° obliquity; perihelion during southern
summer solstice) and a "cold summer orbit" (22.0° obliquity; perihelion during southern winter solstice) for the Southern
Hemisphere. The sensitivity experiments were branched off from a modern orbit simulation (eccentricity=0.0167,
obliquity=23.44, longitude of perihelion=283) after 2,500 model years and integrated for another 500 years to allow the
205 atmospheric dynamics to adapt to the orbital perturbation.

3   Results

3.1   Total organic carbon content

TOC contents and bulk δ^{13}C$_{org}$ data at Site 361 were previously reported by Dummann et al. (2020). Aptian–Albian sediments
at Site 361 range from 0 to 19.7% TOC (Figure 2c and Figure 3a) with marked differences between the three lithostratigraphic
210 units (i.e. black shales, gray, and red beds). Red beds and gray shales generally contain <0.1% TOC and 0.1–2.6% TOC,
respectively, while TOC contents of black shales range from 0.7–19.7% (Figure 3a). Black shale samples with <3% TOC are
generally confined to short interval in core 28 in the top part of black shale unit (Figure 2c) We broadly subdivide the black
shale unit into "low-TOC black shales" (i.e. 0.7–6% TOC) and "high-TOC black shales" (i.e. >6% TOC) to differentiate two
OC burial end-member states and to facilitate the discussion of related changes in paleo-environmental conditions. The former
215 subunit comprises the majority of black shale samples (i.e. 70%), which cluster around a mean of 3.5% TOC (Figure 3a) and
appear to constitute background sedimentation during the Early Aptian (Figure 2c). "High-TOC black shales" contain a broad
range of TOC contents (i.e. 6–19.7%; Figure 3a) and, by contrast, are restricted to narrow (several dm–m thick) and repetitive
stratigraphic intervals (Figure 2c). We note, however, that changes in TOC content across individual high-TOC intervals often
occur gradually and are unrelated to visible changes in sedimentary facies. These observations suggest that both subunits are
220 interrelated and may represent a continuum. As such, the exact placement of the TOC threshold is to some extent arbitrary.

3.2 Sediment composition and provenance

3.2.1 Distribution of K, Si, and Zr

To track changes in geochemical composition related to grain-size and mineralogy of the sediments, we report K/Al, Si/Al and Zr/Al ratios obtained by XRF analysis (Figure 2d–f). All black shales at Site 361 show Si/Al and Zr/Al ratios typical for fine-grained sediments with ratios close to average shale (AS) values (Wedepohl, 2004, 1971) and are distinctly lower than in intercalated turbiditic sandstones (Figure 2e,f and Figure 3b). Neither Si/Al nor Zr/Al ratios differ substantially between high-TOC and low-TOC black shale intervals. In contrast, K/Al ratios vary in concert with TOC (Figure 2d and Figure 3c) with high-TOC black shales showing a higher mean K/Al ratio of 0.39 ± 0.04 ($\bar{x} \pm 1\sigma$) compared to low-TOC black shales with a mean ratio of 0.32 ± 0.05. Turbiditic sandstones show K/Al ratios, which mostly cover the same range as shale samples. Some sandstones, however, show substantially higher K/Al ratios of >0.6 (Figure 3c).

3.2.2 Sediment provenance

Immobile trace element and REE geochemistry were used to constrain the provenance of Early Aptian black shales. To define provenance types and tectonic settings, we used discrimination plots following the approach of Bhatia and Crook (1986) and McLennan et al. (1993), respectively. Furthermore, potential sediment source regions located on the proximal southern African continent were identified based on comparison with geochemical data compiled from the literature. This data compilation comprising shale and mudstone samples from sediment source regions is provided in supplements S2 and S3 and includes all relevant references.

All black shale samples show trace element and REE patterns typical for continental crust with clear differences between low-TOC and high-TOC black shales (Figure 4c–e). Low-TOC black shales show characteristics typical for a recycled sedimentary rock provenance (McLennan et al., 1993), including Th/Sc >1 and enrichment of Zr/Sc relative to Th/Sc (Figure 4c). In addition, all low-TOC samples show Th/Zr and La/Sc ratios indicative for an active continental margin signature (Figure 4d), implying a felsic to intermediate sediment source composition, which is also supported by a strong enrichment of the light REE La, Ce, Pr, Nd, and Sm and a pronounced negative Eu anomaly (Figure 4e). All above proxy parameters overlap with those reported from the Karoo and Cape supergroup (Figure 4c–e).

In contrast, the trace element and REE signature of high-TOC black shales suggests a greater contribution from mafic sediment sources, as indicated by slightly lower Th/Sc ratios (Figure 4c), lower La/Sc ratios (Figure 4d) and depletion of light REE compared to low-TOC black shales (Figure 4e). High-TOC samples plot close to the continental island arc end-member (Figure 4d), indicating a bulk sediment source composition close to granodiorite. Potential source regions comprising mafic rocks include the Kaapvaal Craton and Karoo volcanics (Figure 4c–e).

3.3 Inorganic paleo-redox parameters

3.3.1 Distribution of sulfur and iron

The stratigraphic variation of sulfur content closely parallels that of the TOC content (Figure 5b). Sulfur contents of Early Aptian black shales fluctuate around a mean value of 2.9% ± 1.4% and decrease to 0.4% ± 0.5% in Late Aptian gray shales. Albian red beds are essentially sulfur-free. Low-TOC black shales are characterized by a mean sulfur content of 2.2 ± 0.5%, while high-TOC black shales contain approximately twice as high sulfur contents (4.5 ± 1.6%).

Fe-S-TOC relationships are used to differentiate between paleo-redox states based on diagnostic S/C and S/Fe ratios (Figure 6; Dean and Arthur, 1989; Arthur and Sageman, 1994), the latter of which approximate the degree of pyritization (DOP; Raiswell et al., 1988). Red bed and gray shale samples scatter around a S/C mixing line of ~0.4, typical for sediments deposited in an oxic environment (Berner and Raiswell, 1983; Leventhal, 1983). Gray shales and red beds show S/Fe ratios well below the threshold value of 0.45, which is generally used to discriminate oxic from "restricted" (i.e. suboxic–anoxic) conditions (Raiswell et al., 1988). Black shales show overall higher S/Fe ratios, covering a broader range between the 0.25 and the pyrite line. Low-TOC black shales and high-TOC black shales cluster into two populations with minor overlap. S/Fe ratios of low-TOC black shales fall close to 0.45, with a relatively large scatter between 0.25 and 0.75. High-TOC black shales instead tend to have S/Fe ratios greater than 0.45, often exceeding 0.75 (mean of 0.85 ± 0.24), indicating "inhospitable" (i.e. strictly anoxic to euxinic) conditions (Raiswell et al., 1988).

3.3.2 Distribution of redox-sensitive trace metals

Distribution of the redox-sensitive trace metals (TMs) Ni, Cu, V, and Zn in black shales is presented as TM/Al ratios in Figure 5c–f and enrichment factors (EFs) relative to AS values in Figure 7. All TM/Al ratios co-vary closely with each other and with TOC (Figure 5c–f). Albian red beds all show TM/Al close to or below AS values with mean EFs of 0.7 ± 0.2, 0.9 ± 0.7, 0.8 ± 0.5, and 0.1 ± 0.2 for Ni, Cu, V, and Zn, respectively. Similarly low EFs for V (1.3 ± 0.4) and Zn (1.8 ± 1.4) are present in Late Aptian gray shales, which, however, show substantially higher EFs for Ni (3.4 ± 1.4) and Cu (3.2 ± 1.0). Low-TOC black shales show minor, if any, TM enrichment beyond AS values with mean EFs of 1.2 ± 1.3, 1.3 ± 0.8, 2.0 ± 2.0, and 3.2 ± 5.4 for Ni, Cu, V, and Zn, respectively. In contrast, high-TOC black shales are characterized by consistently higher TM EFs, with V and Zn being particularly enriched as indicated by mean EFs of 10.5 ± 5.9 and 31.4 ± 32.6, respectively. Enrichment of Ni and Cu in high-TOC black shales is more modest with mean values of 4.4 ± 2.2 and 4.5 ± 2.0, respectively.

Cross-plots of TM EFs against TOC provide additional information on the mechanisms of sedimentary TM enrichment and thus paleo-redox conditions (Tribovillard et al., 2006; Algeo and Maynard, 2004). High-TOC black shales show pronounced differences in TM-TOC relationships for Ni, Cu, V, and Zn relative to low-TOC black shales (Figure 7). Ni and Cu EFs tend to increase with TOC content, although only Cu exhibits a clear linear relationship (R^2=0.38) to TOC content. In contrast, V and Zn EFs show a substantial scatter and no relationship to TOC content.

3.4 Biomarker distribution

Our biomarker assessment focusses on thermal maturity, OC sources, and paleo-redox conditions, for which we report selected biomarker parameters, while a detailed discussion of whole suite of biomarkers is beyond the scope of this study.

3.4.1 Thermal maturity

285 Sediments at Site 361 are thermally immature at an estimated R_O of <0.4% (Peters et al., 2007). Steranes mainly possess the thermally least stable $5\alpha,14\alpha,17\alpha(H)$-20R or $5\beta,14\alpha,17\alpha(H)$-20R stereoisomeric configurations. Thermally unstable $17\beta,21\beta(H)$-hopanes dominate over more stable $17\alpha,21\beta(H)$ and $17\beta,21\alpha(H)$ hopanes and the most stable configurations such as $17\alpha,21\beta(H)$-30S-homohopanes and $18\alpha(H)$-22,29,30-trisnorneohopane (Ts) are either absent or occur in trace amounts only. The ratios of $17\beta,21\beta(H)/[17\alpha,21\beta(H)+17\beta,21\alpha(H)+17\beta,21\beta(H)]$-$C_{30}$-hopane ($\beta\beta$-hopane-ratios) vary between

290 0.08 and 0.36 (mean of 0.18 ± 0.06; Figure 8b), do not increase downcore, and show no systematic trend when compared to TOC, indicating that thermal maturation effects had a negligible impact on down-core variations in the biomarker distribution.

3.4.2 Organic carbon sources

Variations in OC sources are assessed based on the relative abundances of n-alkanes, desmethylsteranes, and regular hopanes (i.e. C_{27} and C_{29}–C_{33} hopanes). Chain lengths of n-alkanes range from C_{15} to C_{35}. High molecular weight (HMW) C_{25} to C_{35} n-

295 alkanes show an odd-over-even predominance (with a mean carbon preference index CPI_{25-33} of 1.9; Bray and Evans, 1961), indicating a higher land plant origin (Bray and Evans, 1961; Eglinton and Hamilton, 1967). The ratio of low molecular weight (LMW) C_{15}, C_{17}, and C_{19} n-alkanes, indicative of algal and/or bacterial OC input (Han and Calvin, 1969), to HMW odd carbon-numbered C_{25} to C_{35} n-alkanes varies from 0.2 to 6.7 (Figure 8c). Low-TOC black shales show a lower mean LMW/HMW ratio of 1.3 ± 1.1 compared to high-TOC black shales, which have a mean LMW/HMW ratios of 2.1 ± 1.4.

300 A suite of C_{27} to C_{35} hopanes, reflecting OC inputs from prokaryotic/bacterial sources, and regular C_{27} to C_{30} desmethylsteranes, indicative of eukaryotic OC sources, are present in varying concentrations. Eukaryotic OC generally dominates over bacterial OC, as indicated by sterane/hopane ratios (ratio of C_{27} to C_{29} desmethylsteranes to regular C_{27} and C_{29}–C_{33} hopanes) ranging from 2.3 to 62.5 (Figure 8d). Low-TOC black shales are characterized by mean sterane/hopane ratios of 10.9 ± 9.3, which increase in high-TOC black shale interval to a mean value of 28.3 ± 12.8.

305 The extended 24-n-propylcholestane (24-npc), a proxy that can indicate contributions of marine algae to OC (Moldowan et al., 1990), is present throughout the record. We normalize the abundance of 24-npc to C_{29}-desmethylsterane, which is generally linked to higher land plant inputs (Huang and Meinschein, 1979), to approximate the relative contribution of marine and terrigenous OC. The ratios of 24-npc/C_{29}-sterane co-vary with TOC (Figure 8e) and range between 0.06 and 0.35. Low-TOC black shales show a 24-npc/C_{29}-sterane mean ratio of 0.14 ± 0.08, which increases to 0.21 ± 0.09 in high-TOC black shales.

310 Fractional abundances of regular C_{27}, C_{28}, and C_{29} steranes, depicted as a ternary diagram (Figure 9), are used to differentiate different eukaryotic sources (Huang and Meinschein, 1979). Higher land plant-derived C_{29}-steranes tend to dominate in low-

TOC black shales, while C_{27} and C_{28} dominate over C_{29} in high-TOC black shales, suggesting a greater contribution of marine OC.

3.4.3 Paleo-redox conditions

315 Our molecular paleo-redox assessment is based on the distribution of lycopane, a tail-to-tail linked acyclic isoprenoid, the occurrence of which is limited to anoxic depositional settings (Sinninghe Damsté et al., 2003). Lycopane abundances are normalized to C_{31} *n*-alkane, following Sinninghe Damsté et al. (2003). Lycopane/*n*-C_{31} ratios range from 0.04 to 4.8 and co-vary closely with TOC (Figure 8f), with low-TOC black shales and high-TOC black shales showing mean ratios of 0.7 ± 0.5 and 1.7 ± 1.0, respectively. Furthermore, we screened the aromatic hydrocarbon fraction of all samples for isorenieratene

320 derivatives and related compounds, whose presence imply photic zone euxinia (Koopmans et al., 1996). However, no isorenieratene derivatives were detected in any of the analyzed samples.

4 Discussion

4.1 Temporal trends in organic carbon burial

Changes in OC burial in the Aptian–Albian Cape Basin occurred on different time scales. On a multi-million year time scale,

325 OC burial decreased in two steps, as reflected in the lithological succession of black shales in the Aptian ($6.0 \pm 4.4\%$ TOC), gray shales in the latest Aptian ($0.8 \pm 1.0\%$ TOC), and red beds in the Albian ($<0.1\%$ TOC). Superimposed on this long-term trend, we identify several distinct episodes of enhanced OC burial (i.e. high-TOC black shales), punctuating the Early Aptian interval (Figure 2c). Most of these high-TOC intervals reach peak TOC levels well above 10% ($11.5 \pm 3.2\%$ TOC), clearly separating them from background sedimentation with still elevated but much lower TOC content ($3.5 \pm 1.0\%$ TOC). These

330 high-TOC intervals occurred during different time intervals across the Aptian, including, but not limited to, OAE 1a (Figure 2b,c). The exact duration and the frequency of these intervals is difficult to assess based on the incomplete stratigraphic coverage at Site 361, i.e. they may have lasted longer, and there may have been other high-TOC intervals in non-recovered sediment sections. However, comparable TOC alternations in black shale sequences have been reported from both the North and South Atlantic basins throughout the Cretaceous and have been attributed to geochemical expressions of large-scale

335 climate variations driven by orbital forcing (Beckmann et al., 2005; Behrooz et al., 2018; Hofmann and Wagner, 2011; Wagner et al., 2013; Kolonic et al., 2005; Herrle et al., 2003). To test the impact of orbital forcing on OC burial, we conducted a series of GCM experiments implementing different orbital configuration (i.e. variations in precession and obliquity). The set-up of our GCM is geared to simulate atmospheric processes, including changes in precipitation, run-off, and wind-driven oceanic upwelling, all of which are known to directly or indirectly influence the magnitude of marine OC burial (e.g. Wagner et al.,

340 2013 and references therein). Based on our proxy and GCM results, we provide a depositional model for these episodes of

enhanced OC burial, which is discussed in the context of large-scale reorganizations of tectonic and oceanographic boundary conditions induced by the opening of South Atlantic-Southern Ocean gateways (Dummann et al., 2020).

4.2   Paleo-redox variations

4.2.1   Paleo-redox conditions during black shale deposition in the Early Aptian

345   Early Aptian black shales contain high S contents of 2.9 ± 1.4% (Figure 5b) with S/Fe ratios 0.6 ± 0.3 (Figure 6) and high abundances of the redox-sensitive biomarker lycopane, as reflected in elevated lycopane/n-C_{31} ratios of 1.1 ± 0.9 (Figure 8f), which fall within the range of modern anoxic settings, e.g. oxygen minimum zones along the Peru Margin and the northern Arabian Sea (Sinninghe Damsté et al., 2003). These observations indicate low oxygen concentrations in porewaters and bottom waters during the Early Aptian. S/Fe ratios of ~0.5 (indicating a DOP range of 0.45–0.75, Raiswell et al., 1988) and a limited

350   degree of authigenic TM enrichment (TM EFs close to AS values) in low-TOC black shales suggest overall dysoxic–suboxic conditions during background sedimentation. Consistent with paleo-bathymetric reconstructions (Pérez-Díaz and Eagles, 2017) and sedimentological evidence (Arthur and Natland, 1979), we link reduced oxygen conditions to sluggish deep water ventilation, caused by the narrow and restricted geometry of the Early Aptian Cape Basin. In support of this hypothesis, our GCM results indicate nearly stagnant deep water circulation in the deepest parts of the Cape Basin, where warm and saline

355   waters accumulated (Supplementary Figure 3 in Supplement S4). This halokinetic mode of deep water circulation is generated in all model runs, regardless of implemented climatic boundary conditions (i.e. pCO$_2$ levels of 600 and 1200 ppm; Supplementary Figure 3 in Supplement S4), indicating that it represents a persistent feature of South Atlantic overturning circulation during the Early Aptian.

Anoxia intensified during high TOC intervals, as indicated by (1) a doubling of sulfur contents (Figure 5b), (2) sharp increases

360   in redox sensitive TM/Al ratios (Figure 5c–f), and (3) elevated lycopane/n-C_{31} ratios (Figure 8f). Furthermore, Fe-S-TOC relationships show that most of high-TOC black shales have S/Fe ratios greater than 0.75 (Figure 6), arguing for strictly anoxic–euxinic conditions (Raiswell et al., 1988). Distinguishing euxinic conditions, characterized by accumulation of H$_2$S in the water column, from non-sulfidic but anoxic ('ferruginous') conditions is difficult based on Fe-S-TOC systematics alone. The distribution of redox-sensitive TMs, however, may serve to distinguish these subtle fluctuations at the extreme end of the redox

365   scale (Algeo and Maynard, 2004; Tribovillard et al., 2006; Meyer and Kump, 2008).

At Site 361, all analyzed redox-sensitive TMs show close parallel trends of enrichment and depletion concurrent with TOC variations (Figure 5). This strong similarity of trends between different redox-sensitive TMs supports that changes in the dissolved TM inventory are negligible and that paleo-redox conditions exerted the dominant control over TM enrichment (Algeo and Maynard, 2008). Cross-plots of TM EFs and TOC reveal two distinct patterns of TM enrichment for Ni and Cu and V and Zn in high-TOC black shales (Figure 7). Ni and Cu EFs increase in parallel with TOC content, suggesting that

370   excess TM enrichment was controlled by OC supply to the sediment. Such a coupling of Ni and Cu enrichment with OC flux has been observed in sediments deposited under both anoxic ferruginous conditions as well as euxinic conditions (Algeo and

Maynard, 2004; Tribovillard et al., 2006) and mainly stems from their behavior as micronutrients (Tribovillard et al., 2006; Little et al., 2015). In contrast, high-TOC black shales are characterized by substantial enrichment of V, which is decoupled from OC input, as indicated by the lack of correlation between V EFs and TOC (Figure 7c). This mode of V enrichment supports euxinic conditions at the sediment-water interface and possibly the (lower) water column (Algeo and Maynard, 2004; Tribovillard et al., 2006). The presence of free H_2S favors reduction to V(III) (Wanty and Goldhaber, 1992), which forms insoluble hydroxide-phases that can precipitate in quantity from the water column and/or the sediment-water interface, leading to a decoupling of V supply from OC flux. Zn EFs exhibit a distribution similar to V EFs (Figure 7d), which is typical for euxinic settings and potentially results from the formation of independent ZnS phases at the sediment/water interface (Algeo and Maynard, 2004). Further evidence for euxinic conditions during high-TOC intervals comes from the occurrence of type IIS kerogens (Hartwig et al., 2012), indicating excess availability of sulfur.

In contrast to many Mesozoic black shales deposited under euxinic conditions (Meyer and Kump, 2008 and references therein), high-TOC black shales at Site 361, however, do not contain biomarkers derived from phototrophic H_2S oxidizing bacteria (i.e. isorenieratene derivatives and other aryl isoprenoids; Koopmans et al., 1996). This general lack of photic zone euxinia-indicating compounds at Site 361 puts constraints on the extent of water column euxinia and suggests that H_2S did not pervade into the upper water column. The oceanographic conditions that favored this limited extent of euxinia are difficult to assess based on the data presented here. However, our GCM results indicate relatively vigorous overturning at intermediate water depths in the Cape Basin (i.e. <1,000 m; Supplementary Figure 3 in Supplement S4). These water masses, which have previously been identified and referred to as "South Atlantic intermediate waters" by Dummann et al. (2020), may have caused an efficient ventilation at intermediate water depths, thereby providing a barrier for upward migration of H_2S into shallow waters.

4.2.2   Early Aptian–Albian long-term increase in seawater oxygenation

Early Aptian black shales were replaced by Late Aptian gray shales and Albian red beds (Figure 2c), reflecting a decrease in OC burial over at least 13 Ma (Gradstein et al., 2012). Our multi-proxy paleo-redox data suggest that this long-term decline in OC burial was accompanied by major redox changes in the deep Cape Basin. Evidence includes (1) a stepwise decrease in sulfur concentrations (Figure 5b), (2) shifts in Fe-S-TOC relationships with decreasing S/Fe ratios (Figure 6), (3) a decrease in redox-sensitive trace element enrichment, in particular of V and Zn (Figure 5c–f), and (4) decreasing lycopane/n-C_{31} ratios (Figure 8f; Sinninghe Damsté et al., 2003). These results are consistent and suggest a two-step shift from suboxic–anoxic/euxinic to suboxic and oxic conditions, respectively, which was caused by a strengthening of deep water ventilation due the progressive opening of two South Atlantic-Southern Ocean gateways located on the Falkland Plateau and in the Georgia Basin, as indicated by a recent study based on Nd-isotope data and ocean current simulations (Dummann et al., 2020). It is noteworthy, however, that Late Aptian gray shales show relatively high EFs of Ni and Cu, but not the other TMs (Figure 5c–f). Taking above lines of evidence into account, we consider it unlikely that this enrichment stems from redox-related authigenic processes, but rather suggests additional processes supplying micro-nutrients to Late Aptian sediments in the Cape

Basin through detrital input (Garver et al., 1996) or scavenging by biogenic silica (Böning et al., 2015; Twining et al., 2012). The exact mechanism, however, remains to be identified.

4.3   Composition of organic carbon in Early Aptian black shales

Both, low TOC and high-TOC black shales contain thermally immature OC, as indicated by the continuous down-core presence of 5β-steranes and 17β,21β-hopanes. ββ-Hopane ratios do not increase downcore and show no systematic trend with TOC (Figure 8b). Hence, changes in the sterane and hopane biomarker distribution due to thermal maturation are negligible and are interpreted to reflect primary variations in the source and/or preservation of OC.

Early Aptian low-TOC background sediments contain a mixture of marine and terrestrial OC with a greater proportion of terrestrial OC compared to high-TOC black shale intervals, as indicated by (1) lower LMW/HMW n-alkane ratios (Figure 8c), (2) lower sterane/hopane ratios (Figure 8d) indicating a higher contribution from bacteria, typical for land-derived OC (e.g. Moldowan et al., 1985), (3) lower 24-npc/C_{29}-sterane ratios (Figure 8e), and (4) higher abundances of C_{29}-sterane (Figure 9). These results are consistent with previously published Rock-Eval data that show a dominance of terrigenous type III kerogen in low-TOC black shales (Hartwig et al., 2012).

In contrast, high-TOC black shales mainly comprise marine OC, as indicated by the dominance of LMW n-alkanes (Figure 8c). In connection with high sterane/hopane ratios (Figure 8d), the dominance of algal C_{27}-sterane and C_{28}-sterane over higher land plant-derived C_{29}-sterane support a predominantly marine OC source (Figure 9; Huang and Meinschein, 1979; Moldowan et al., 1985). Increased 24-npc/C_{29}-sterane ratios similarly suggest enhanced input of marine OC (Figure 8e), as 24-npc has been linked to OC inputs from chrysophyte algae (Moldowan et al., 1990) and/or Rhizaria (Nettersheim et al., 2019), a group of heterotrophic unicellular protists, including foraminifera and radiolaria that occurs ubiquitously in the global ocean and plays a key in the export of carbon from the photic zone to sediments (Caron, 2016; Lampitt et al., 2009). Based on above lines of evidence, we conclude that high-TOC black shales mark episodes of enhanced productivity and preservation of marine OC in the Cape Basin. This is further supported by the occurrence of II and IIS kerogens with hydrogen index values of up to 700 mg g^{-1} TOC in high-TOC black shales (Herbin et al., 1987; Hartwig et al., 2012).

4.4   Depositional processes and provenance of Early Aptian black shales

Early Aptian black shales are intercalated with abundant sandstones, sandy mudstones, and siltstones (Figure 2a), which represent turbidites deposited in a fan to fan-valley environment (The Shipboard Scientific Party, 1978; Natland, 1978). This raises the question as to whether high-TOC/low-TOC alternations reflect changes between turbiditic and hemipelagic sedimentation, similar to those observed at numerous sites in the opening North Atlantic and South Atlantic basins (Degens et al., 1986; Forster et al., 2008). Our geochemical grain-size proxies (i.e. Si/Al and Zr/Al ratios), however, indicate a homogenous grain-size among all investigated shale samples with a markedly higher abundance of fine-grained siliciclastic material compared to sandstones (Figure 3b). These observations and the good reproducibility of global $\delta^{13}C$ variations

recorded in black shales at Site 361 (Figure 2b; Dummann et al., 2020) suggest that both black shale types are of hemipelagic origin.

Immobile trace element and REE data suggest that high-TOC/low-TOC alternations were accompanied by consistent changes in sediment provenance, which we attribute to changes in sediment routing and weathering regime on the proximal southern African continent. Similar to today, sediments accumulating in the deep Cape Basin were most likely transported to the SW African shelf by west-flowing river systems (De Wit, 1999; Dingle and Hendry, 1984; Partridge and Maud, 1987). According to paleo-drainage reconstructions, one major sediment route may have been the paleo-Karoo River, which entered the S-Atlantic close to the modern Olifants river mouth in close proximity to Site 361 (Figure 4a; De Wit, 1999). Recent apatite fission-track analyses support these paleo-drainage reconstructions and date the incision of the paleo-Karoo River into coastal areas of SW Africa at ~120 to ~110 Ma (Kounov et al., 2008), implying active river input to the Aptian Cape Basin. We consider three potential sediment source regions, representing the major geological provinces of the southern African continent (Figure 4a): (1) Paleozoic to Early Mesozoic sediments from the Karoo and Cape supergroup, mainly located in the SW and central part of S-Africa, (2) Jurassic volcanics related to the Karoo large igneous province, capping and intervening the Karoo supergroup in the E and NE, and (3) Archean to Proterozoic sedimentary, volcanic, and metamorphic rocks of the Kaapvaal Craton, located in the NE. The geochemical composition of potential sediment source regions is presented in Figure 4c–e. Due to the complex geology of the Kaapvaal Craton and related intracratonic sediment sequences, we also included geochemical data of river bed sediments from modern rivers draining the Kaapvaal Craton, reflecting a more integrated signal (Garzanti et al., 2014).

Trace element discrimination plots suggest that Paleozoic sediments from the Karoo and Cape supergroup were the dominant weathering source of low-TOC black shales (Figure 4c–e). This indicates a minor contribution from the Kaapvaal Craton and Karoo volcanics in the E and NE, which display more mafic geochemical signatures, as indicated by lower Th/Sc, Zr/Sc, La/Sc, higher Ti/Zr (Figure 4c,d) and light REE depletion (REE characteristics of the Kaapvaal Craton are approximated by average Archean upper crust composition; Figure 4e). Hence, we propose a dominant sediment input from Paleozoic source regions located along the coast in the W and SW, with a minor contribution from mafic rocks further inland. Similar coastal regions have been inferred as the source region of turbiditic sediments at Site 361 (Natland, 1978). This may indicate that sediment input during low-TOC background sedimentation predominantly originated from areas located W of the escarpment (Figure 4a), which today represents a major drainage divide that possibly already existed during the Early Cretaceous (Moore et al., 2009).

In contrast, trace element and REE compositions of high-TOC black shales support a shift to more mafic signatures, typical for the Kaapvaal Craton and/or Karoo volcanics (Figure 4c–e), suggesting enhanced sediment supply from the N and NE (Figure 4a). These data indicate a stronger sediment supply from areas located in the continent's interior relative to more coastal areas. Based on this trend, we propose that the shift in provenance from low- to high-TOC black shales reflects enhanced moisture supply to the continent's interior, augmenting river run-off in the upstream regions of west-flowing river systems (e.g. the paleo-Karoo River) and/or increasing chemical weathering intensity of basaltic rocks.

High-TOC black shales display overall high K/Al ratios of ~0.4 (Figure 2d), characteristic for illite (Figure 4b; Weaver and Pollard, 1973). Consistent with their more mafic trace element signature, the Kaapvaal Craton and Karoo volcanics show K/Al ratios substantially lower than those recorded in high-TOC black shales (Figure 4b), indicating that higher K/Al ratios cannot be explained by the change in sediment provenance proposed for high-TOC black shales. Instead, we link K/Al ratios to a change in the weathering intensity of K-rich source regions along the coast (i.e. located west of the escarpment), including argillaceous sediments of the Karoo and Cape supergroups, Cape Granites, and pan-African terranes of the Saldania Belt (Figure 4a). Today, rivers draining these felsic rocks supply erosional inputs particularly rich in illite, which accounts for up to 90% of the total clay mineral assemblage in surface sediments near their river mouths (Birch, 1978). Quaternary sediment records also show that strong physical erosion and increased fluvial activity in these coastal source regions are reflected in enhanced input of K to the SW African shelf (Hahn et al., 2016), and probably the deep southern Cape Basin (Dickson et al., 2010). Assuming analogous mechanisms for the Cretaceous, we propose that the recorded increases in K/Al ratios at Site 361 reflect periods of strong physical erosion of coastal K-rich source regions and riverine discharge to the Cape Basin. Supporting evidence comes from the good agreement of K/Al ratios of high-TOC black shales and unweathered Karoo sediments (Figure 4b), suggesting efficient bedrock erosion with minor alteration of the sediment's chemical composition by weathering during transport from source to sink.

Based on above lines of evidence, we propose that high-TOC black shales were deposited during episodes of enhanced precipitation and strong river run-off from the proximal S-African continent, which caused enhanced contribution of weathering inputs from the continent's interior and intensification of bedrock erosion along the coast.

4.5 Climate simulations

In order to test feedback mechanisms on OC burial in the young South Atlantic basin, we modeled atmospheric and oceanographic circulation changes, specifically changes in wind-driven upwelling and continental hydrology (i.e. precipitation and total run-off) in response to orbital variations and pCO$_2$ changes. Our model results indicate that Site 361 and the southern African continent were located within the humid austral westerly wind belt (Figure 10a). Even though the strong N–S gradient in annual mean precipitation across Africa makes this result sensitive to the applied paleogeography, the paleo-climatic setting of southern African simulated in our model is consistent with previous GCM experiments (Chaboureau et al., 2012). It is further supported by the Early Cretaceous distribution of climate-sensitive deposits on the African continent, which is characterized by a dominance of evaporites north of a paleo-latitude of ~40° S and coal deposits south of ~40° S, reflecting overall arid and humid conditions, respectively (Figure 1; Boucot et al., 2013; Chumakov et al., 1995). This distribution implies that the descending limb of the southern paleo-Hadley Cell separating the subtropical arid climate belt and the mid-latitude humid climate belt was located north of Site 361 (Boucot et al., 2013; Chumakov et al., 1995). In accordance with this pattern, the simulated zonal mean edge of the Southern Hemisphere Hadley Cell (defined as the latitude of the first zero crossing of the atmospheric mass stream function at the 500 hPa level) is located at around 31° S and 32° S for the 600 and 1200 ppm experiments, respectively. This position is consistent with sparse geochemical data from Early Cretaceous (Albian) black shale

sections from DSDP Site 530 in the Angola Basin and DSDP Site 511 on the Falkland Plateau at paleo-latitudes of ~37° S and ~58° S, respectively (Wagner et al., 2013).

In contrast to the modern location along the coast of SW Africa, which is strongly influenced by the Benguela upwelling system, our simulations indicate no large-scale upwelling system along the SW African margin during the Aptian (Supplementary Figure 4 in Supplement S4). We note, however, that we cannot rule out small coastal upwelling cells on scales below the horizontal model resolution of ~200 km. The absence of large-scale upwelling is a direct consequence of the more poleward position of the southern tip of Africa in the Early Cretaceous and the associated change in the dominant large-scale wind regime. While the present-day Benguela upwelling is driven by the prevailing southeasterly trade winds under the subtropical limp of the Hadley Cell, the more southern position of the African continent during the Aptian leads to the predominance of the mid-latitude westerlies. An eastern boundary upwelling system is, however, simulated further to the north in the Angola Basin, even though its strength would have been limited by the dimensions of the small basin. Based on these results, we conclude that coastal upwelling had a negligible impact on the magnitude of OC burial at Site 361.

Our simulations further indicate minor alterations in continental hydrology in response to changes in atmospheric pCO$_2$ levels (at a constant orbital configurations). At 600 ppm pCO$_2$, annual mean precipitation over southern Africa (i.e. in an area we consider representative for the catchment area based on our sediment provenance assessment; Figure 10a) accounts to 3 mm d^{-1}. A doubling of atmospheric pCO$_2$ leads to overall higher precipitation south of Site 361 but drier conditions in the subtropical regions further north (Figure 10b). This is in line with an enhanced hydrological cycle as consequence of increased atmospheric pCO$_2$ and global mean temperature (Held and Soden, 2006). As southern Africa is influenced by both regional aridification in its subtropical northern part and enhanced precipitation to the South, annual mean rainfall averaged over the proposed catchment area only increases by 1% between both simulations (Figure 11a). However, we note that the doubling in pCO$_2$ leads to a more pronounced seasonal cycle in the local rainfall (Figure 11a and Supplementary Figure 5 in Supplement S4) with reduced precipitation in austral summer (i.e. November–May) and an increase during the austral winter (i.e. June–August).

In contrast, changes in orbital configuration exert a more profound control on continental hydrology over southern Africa. The "cold summer orbit" (i.e. 22.0° obliquity, perihelion during southern winter solstice) is associated with an increase of annual mean precipitation of 14% over the proposed catchment area (Figure 10c and Figure 11a) compared to the "warm summer orbit" (24.5° obliquity, perihelion during southern summer solstice), which causes an increase in total annual run-off of 31-35% (Figure 11b). This disproportional increase in run-off relative to precipitation may in part be related to the colder summer temperatures (~5 °C difference between both orbital configurations during February), which causes a reduced evaporation of precipitation. Highest seasonal variability in total run-off is simulated during March to May (Figure 11b) with fluxes two to three times higher for the "cold summer orbit". In "warm summer orbit" simulations, precipitation is particularly strong along the SW coast of Africa (Supplementary Figures 6 and 7 in Supplement S4), implying that sediment production and mobilization predominantly occurred in coastal areas, which is consistent with provenance data from low-TOC black shales. Increased precipitation associated with a "cold summer orbit" is not limited to the coastal regions, but also simulated further inland with

highest variability during austral summer and autumn (Supplementary Figures 6 and 7 in Supplement S4). We note that the large spatial extent of the enhanced moisture supply reduces the influence of uncertainties in the exact placement of the proposed catchment area for the significance of our results. Importantly, we show that the simulated run-off sensitivity to changes in the orbital parameters is very similar during low and high atmospheric pCO_2 model runs (Figure 11b and Supplementary Figures 6 and 7 in Supplement S4), which suggests a similar response of continental hydrology to orbital forcing during different parts of the Aptian (i.e. before, during, and after OAE 1a).

4.6   Depositional model for OC burial

Internal heterogeneities in OC quantity and composition of Early Aptian black shales at Site 361, reflected in alternations between high-TOC and low-TOC intervals, suggest recurrent modulations of OC burial on time scales well below 1 Myr. Geochemical characteristics of all high-TOC intervals at Site 361 imply comparable depositional conditions with regard to paleo-redox conditions, OC source, and sediment provenance. High-TOC black shales were deposited during episodes of enhanced production and preservation of marine OC under anoxic–euxinic conditions, accompanied by changes in provenance and weathering state of sediments delivered from the proximal southern African continent. The latter are interpreted to reflect an expansion of the catchment area in response to enhanced precipitation in the continent's interior and intense bedrock erosion along the coast due to increased river run-off. Based on our GCM results, we propose that orbitally driven fluctuations in continental hydrology (i.e. precipitation and run-off), in particular minima in obliquity and a perihelion during southern winter solstice causing colder summers, triggered the episodic recurrence of conditions conducive to enhanced burial of OC in the Cape Basin. Our results indicate a similar response of continental hydrology to orbital forcing at 600 ppm and 1200 ppm, which may explain the similar OC burial response during all high-TOC intervals before, during, and after OAE 1a. Unfortunately, the incomplete stratigraphic coverage at Site 361 prevents us from constraining the timing, duration, and pacing of high-TOC intervals and their link to orbital forcing. We therefore suggest establishing an orbital chronology for the Early Cretaceous sedimentary record of the Cape Basin to test our hypothesis once new, high-resolution sediment records from the study area become available.

4.7   Wider implications

Our study re-emphasizes that ocean basins emerging during the break up of super-continents provided favorable conditions for enhanced OC burial through basin geometries promoting hydrographic isolation and a close coupling of atmosphere–land–ocean interactions. The results of this study further suggest that deep marine environments (i.e. >2,000 m) along the continental margins of emerging ocean basins were sensitive to changes in nutrient fluxes from the continent. In case of the Cape Basin, this close land-ocean coupling is supported by our model results, which suggest that no large-scale ocean upwelling occurred along the SW African margin during the Aptian (Supplementary Figure 4 in Supplement S4). One underlying reason for this higher sensitivity to across-shelf nutrient transport in young ocean basins may have been very narrow shelves, permitting substantial and almost direct escape of continent-derived nutrients and mineral matter to the deep ocean, which is supported

570   by recent modeling data (Sharples et al., 2017; Izett and Fennel, 2018). Shelves in emerging ocean basins are generally narrow and underdeveloped, as some time is required for drainage systems to mature and marginal strata to accumulate (Ravnås and Steel, 1998; Trabucho Alexandre et al., 2012). Consistent with these characteristics, turbiditic sandstones deposited at Site 361 lack re-deposited benthic organisms, which has been interpreted to reflect short residence times or even no intermediate storage in near-shore or shelf environments.

575   Our GCM results further indicate that southern Africa was located South of the descending limb of the Hadley Cell and influenced by the austral westerlies. These results serve to constrain the position of the descending limb of the southern Hadley Cell during the Early Cretaceous, which had proven difficult based on previously available data and coring sites (Wagner et al., 2013). The results suggest a close coupling of marine OC burial dynamics and orbitally paced atmospheric processes operating beneath the Ferrell Cell, similar to what has been observed at sites beneath the Hadley Cell (Wagner et al., 2013).

580 **5   Conclusions**

In this study, we reconstruct the evolution of paleo-redox conditions, OC composition, and sediment provenance in the Aptian–Albian Cape Basin based on Fe-S-TOC systematics, distribution of redox-sensitive trace metals, lipid biomarker data, and the inorganic geochemical composition of sediments at Site 361. The results demonstrate that hydrographic restriction of the Cape Basin during the Early Aptian generally promoted oxygen-deficiency in the deeper water column, favoring the deposition of

585   extensive black shales. The richness and composition of OC in Early Aptian black shales at Site 361 varied on time scales <1 Myr, documented in high-TOC (6–20%) black shale intervals, which occur repetitively throughout the records. These high-TOC intervals were the result of enhanced burial of marine OC deposited under anoxic, and probably euxinic bottom water conditions. Changes in OC burial were tightly coupled to fluctuations in river run-off from the southern African continent, suggesting orbitally driven aridity/humidity variations in the mid-latitude humid climate zone as primary forcing mechanism.

590   Based on this tight coupling of biogeochemical cycling in the deep (>2,000 m) Cape Basin and climate–land–ocean interactions, we propose that narrow immature continental shelves in emerging ocean basin facilitated a more efficient land–open ocean nutrient transfer. By Late Aptian–Albian times, the abatement of hydrographic restriction of the Cape Basin terminated the conditions favorable for OC preservation, as reflected in a two-step increase in bottom water oxygenation and concomitant decreases in OC burial, indicating that intensified deep water ventilation decreased the sensitivity of the basin to

595   climatic perturbations. This leads us to conclude that climatic fluctuations alone without the appropriate basin configuration for OC preservation were insufficient to generate enhanced OC burial.

6   Data availability

All original data of this publication will be made available through PANGAEA® Data Publisher for Earth and Environmental Science (https://www.pangaea.de/).

7 Author contributions

PH, SF, JOH, JR, and TW were involved in the conceptualization of this study and acquired funding. WD and PH conducted XRF analyses. Biomarker analysis were conducted by WD under supervision of SK, CH, and JR. ICP-MS data were acquired by ML under supervision of HUK. SS and SF carried out the modeling experiments. WD integrated the data and wrote the manuscript with contributions from all authors.

8 Competing interests

The authors declare that they have no conflict of interest.

9 Acknowledgments

We thank Nicole Mantke and Simon Kalinowski for their support in proxy data acquisition and Tamara Mai for her help during sampling of Site 361. Model integrations were conducted at the Computing Center of Kiel University. We thank Janine Blöhdorn for generating most of the Cretaceous KCM boundary conditions and Stefan Hagemann for constructing the parameters for the hydrological discharge model. This research used samples provided by the Deep Sea Drilling Project. PH, JOH and SF received funding for this work from the German Research Foundation DFG (grant numbers HO2188/9, HE3521/6).

10 References

Algeo, T. J., and Maynard, J. B.: Trace-element behavior and redox facies in core shales of Upper Pennsylvanian Kansas-type cyclothems, Chemical Geology, 206, 289-318, https://doi.org/10.1016/j.chemgeo.2003.12.009, 2004.

Algeo, T. J., and Maynard, J. B.: Trace-metal covariation as a guide to water-mass conditions in ancient anoxic marine environments, Geosphere, 4, 872-887, https://doi.org/10.1130/GES00174.1, 2008.

Arthur, M. A., and Natland, J. H.: Carbonaceous sediments in the North and South Atlantic: The Role of Salinity in Stable Stratification of Early Cretaceous Basins, in: Deep Drilling Results in the Atlantic Ocean: Continental Margins and Paleoenvironment, edited by: Talwani, M., Hay, W. W., and Ryan, W. B. F., Maurice Ewing Series, 3, American Geophysical Union, Washington DC (USA), 375-401, https://doi.org/10.1029/me003p0375, 1979.

Arthur, M. A., and Sageman, B. B.: Marine Black Shales: Depositional Mechanisms and Environments of Ancient Deposits, Annual Review of Earth and Planetary Sciences, 22, 499-551, https://doi.org/10.1146/annurev.ea.22.050194.002435, 1994.

Beckmann, B., Flögel, S., Hofmann, P., Schulz, M., and Wagner, T.: Orbital forcing of Cretaceous river discharge in tropical Africa and ocean response, Nature, 437, 241-244, https://doi.org/10.1038/nature03976, 2005.

Behrooz, L., Naafs, B. D. A., Dickson, A. J., Love, G. D., Batenburg, S. J., and Pancost, R. D.: Astronomically driven variations in depositional environments in the South Atlantic during the Early Cretaceous, Paleoceanography and Paleoclimatology, 33, 894-912, https://doi.org/10.1029/2018pa003338, 2018.

630 Berger, A.: Long-term variations of daily insolation and Quaternary climatic changes, Journal of the atmospheric sciences, 35, 2362-2367, https://doi.org/10.1175/1520-0469(1978)035<2362:LTVODI>2.0.CO;2, 1978.

Berner, R. A., and Raiswell, R.: Burial of organic carbon and pyrite sulfur in sediments over Phanerozoic time: a new theory, Geochim Cosmochim Ac, 47, 855-862, https://doi.org/10.1016/0016-7037(83)90151-5, 1983.

Bhatia, M. R., and Crook, K. A.: Trace element characteristics of graywackes and tectonic setting discrimination of sedimentary basins,
635 Contributions to Mineralogy and Petrology, 92, 181-193, https://doi.org/10.1007/bf00375292, 1986.

Birch, G.: The distribution of clay minerals on the continental margin off the West Coast of South Africa, Transactions of the Geological Society of South Africa, 81, 23-24, 1978.

Böning, P., Shaw, T., Pahnke, K., and Brumsack, H.-J.: Nickel as indicator of fresh organic matter in upwelling sediments, Geochim Cosmochim Ac, 162, 99-108, https://doi.org/10.1016/j.gca.2015.04.027, 2015.

640 Boucot, A. J., Xu, C., Scotese, C. R., and Morley, R. J.: Phanerozoic Paleoclimate: An Atlas of Lithologic Indicators of Climate, SEPM Concepts in Sedimentology and Paleontology, 11, SEPM Society for Sedimentary Geology, Tulsa (USA), 30 pp., https://doi.org/10.2110/sepmcsp.11, 2013.

Bralower, T. J., and Thierstein, H. R.: Low productivity and slow deep-water circulation in mid-Cretaceous oceans, Geology, 12, 614-618, https://doi.org/10.1130/0091-7613(1984)12<614:LPASDC>2.0.CO;2, 1984.

645 Bray, E., and Evans, E.: Distribution of n-paraffins as a clue to recognition of source beds, Geochim Cosmochim Ac, 22, 2-15, https://doi.org/10.1016/0016-7037(61)90069-2, 1961.

Cao, W., Zahirovic, S., Flament, N., Williams, S. E., Golonka, J., and Muller, R. D.: Improving global paleogeography since the late Paleozoic using paleobiology, Biogeosciences, 14, 5425-5439, https://doi.org/10.5194/bg-2017-94-ac1, 2017.

Cao, W., Williams, S., Flament, N., Zahirovic, S., Scotese, C., and Müller, R. D.: Palaeolatitudinal distribution of lithologic indicators of
650 climate in a palaeogeographic framework, Geological Magazine, 156, 331-354, https://doi.org/10.1017/s0016756818000110, 2019.

Caron, D. A.: The rise of Rhizaria, Nature, 532, 444-445, https://doi.org/10.1038/nature17892, 2016.

Chaboureau, A.-C., Donnadieu, Y., Sepulchre, P., Robin, C., Guillocheau, F., and Rohais, S.: The Aptian evaporites of the South Atlantic: a climatic paradox?, Clim Past, 9, 1047-1058, https://doi:10.5194/cp-8-1047-2012, 2012.

Chumakov, N. M., Zharkov, M. A., Herman, A. B., Doludenko, M. P., Kalandadze, N. N., Lebedev, E. L., Ponomarenko, A. G., and Rautian,
655 A. S.: Climatic belts of the mid-Cretaceous time, Stratigraphy and Geological Correlation, 3, 241-260, 1995.

Coccioni, R., Erba, E., and Premoli-Silva, I.: Barremian-Aptian calcareous plankton biostratigraphy from the Gorgo Cerbara section (Marche, central Italy) and implications for plankton evolution, Cretaceous Research, 13, 517-537, https://doi.org/10.1016/0195-6671(92)90015-I, 1992.

Croudace, I. W., and Rothwell, R. G.: Micro-XRF Studies of Sediment Cores: Applications of a non-destructive tool for the environmental
660 sciences, Springer, Heidelberg (Germany), 650 pp., 2015.

Crowley, T. J., Yip, K. J. J., and Baum, S. K.: Milankovitch cycles and Carboniferous climate, Geophysical Research Letters, 20, 1175-1178, https://doi.org/10.1029/93GL01119, 1993.

De Wit, M.: Post-Gondwana drainage and the development of diamond placers in western South Africa, Economic Geology, 94, 721-740, https://doi.org/10.2113/gsecongeo.94.5.721, 1999.

665   Dean, W. E., and Arthur, M. A.: Iron-sulfur-carbon relationships in organic-carbon-rich sequences I: Cretaceous Western Interior Seaway, American Journal of Science, 289, 708-743, https://doi.org/10.2475/ajs.289.6.708, 1989.

Degens, E. T., Emeis, K. C., Mycke, B., and Wiesner, M. G.: Turbidites, the principal mechanism yielding black shales in the early deep Atlantic Ocean, in: North Atlantic Palaeoceanography, edited by: Summerhayes, C. P., and Shackleton, N. J., Special Publications, 21, Geological Society of London, London (UK), 361-376, https://doi.org/10.1144/gsl.sp.1986.021.01.26, 1986.

670   Dickson, A. J., Leng, M. J., Maslin, M. A., and Röhl, U.: Oceanic, atmospheric and ice-sheet forcing of South East Atlantic Ocean productivity and South African monsoon intensity during MIS-12 to 10, Quaternary Science Reviews, 29, 3936-3947, https://doi.org/10.1016/j.quascirev.2010.09.014, 2010.

Dingle, R. V., and Hendry, Q. B.: Late Mesozoic and Tertiary sediment supply to the eastern Cape Basin (SE Atlantic) and palaeo-drainage systems in southwestern Africa, Marine Geology, 56, 13-26, 1984.

675   Donnadieu, Y., Pucéat, E., Moiroud, M., Guillocheau, F., and Deconinck, J.-F.: A better-ventilated ocean triggered by Late Cretaceous changes in continental configuration, Nature Communications, 7, 10316, https://doi.org/10.1038/ncomms10316, 2016.

Dulski, P.: Reference materials for geochemical studies: New analytical data by ICP-MS and critical discussion of reference values, Geostandards Newsletter, 25, 87-125, https://doi.org/10.1111/j.1751-908x.2001.tb00790.x, 2001.

Dummann, W., Steinig, S., Hofmann, P., Flögel, S., Osborne, A. H., Frank, M., Herrle, J. O., Bretschneider, L., Sheward, R. M., and Wagner,
680   T.: The impact of Early Cretaceous gateway evolution on ocean circulation and organic carbon burial in the emerging South Atlantic and Southern Ocean basins, Earth Planet Sc Lett, 530, 115890, https://doi.org/10.1016/j.epsl.2019.115890, 2020.

Eglinton, G., and Hamilton, R. J.: Leaf epicuticular waxes, Science, 156, 1322-1335, https://doi.org/10.1126/science.156.3780.1322, 1967.

Erba, E.: Nannofossils and superplumes: the early Aptian "nannoconid crisis", Paleoceanography, 9, 483-501, https://doi.org/10.1029/94PA00258, 1994.

685   Forster, A., Kuypers, M. M., Turgeon, S. C., Brumsack, H.-J., Petrizzo, M. R., and Sinninghe Damsté, J. S.: The Cenomanian/Turonian oceanic anoxic event in the South Atlantic: New insights from a geochemical study of DSDP Site 530A, Palaeogeography, Palaeoclimatology, Palaeoecology, 267, 256-283, https://doi.org/10.1016/j.palaeo.2008.07.006, 2008.

Garver, J. I., Royce, P. R., and Smick, T. A.: Chromium and nickel in shale of the Taconic foreland; a case study for the provenance of fine-grained sediments with an ultramafic source, Journal of Sedimentary Research, 66, 100-106, https://doi.org/10.1306/d42682c5-2b26-11d7-
690   8648000102c1865d, 1996.

Garzanti, E., Padoan, M., Setti, M., López-Galindo, A., and Villa, I. M.: Provenance versus weathering control on the composition of tropical river mud (southern Africa), Chemical Geology, 366, 61-74, https://doi.org/10.1016/j.chemgeo.2013.12.016, 2014.

Govindaraju, K.: 1994 Compilation of working values and sample description for 383 geostandards, Geostandards Newsletter, 18, 1-158, https://doi.org/10.1046/j.1365-2494.1998.53202081.x-i1, 1994.

695   Gradstein, F. M., Ogg, J. G., Schmitz, M., and Ogg, G.: The Geologic Time Scale 2012, Elsevier, Amsterdam, Netherlands, 1176 pp., https://doi.org/10.1016/c2011-1-08249-8, 2012.

Hahn, A., Compton, J. S., Meyer-Jacob, C., Kirsten, K. L., Lucasssen, F., Mayo, M. P., Schefuß, E., and Zabel, M.: Holocene paleo-climatic record from the South African Namaqualand mudbelt: A source to sink approach, Quaternary International, 404, 121-135, https://doi.org/10.1016/j.quaint.2015.10.017, 2016.

700   Han, J., and Calvin, M.: Hydrocarbon distribution of algae and bacteria, and microbiological activity in sediments, Proceedings of the National Academy of Sciences, 64, 436-443, https://doi.org/10.1073/pnas.64.2.436, 1969.

Hartwig, A., di Primio, R., Anka, Z., and Horsfield, B.: Source rock characteristics and compositional kinetic models of Cretaceous organic rich black shales offshore southwestern Africa, Org Geochem, 51, 17-34, https://doi.org/10.1016/j.orggeochem.2012.07.008, 2012.

705 Held, I. M., and Soden, B. J.: Robust responses of the hydrological cycle to global warming, Journal of Climate, 19, 5686-5699, https://doi.org/10.1175/jcli3990.1, 2006.

Herbin, J. P., Muller, C., de Graciansky, P. C., Jacquin, T., Magniez-Jannin, F., and Unternehr, P.: Cretaceous anoxic events in the South Atlantic, Revista Brasileira de Geociências, 17, 92-99, https://doi.org/10.25249/0375-7536.19879299, 1987.

Herrle, J. O., Pross, J., Friedrich, O., Kößler, P., and Hemleben, C.: Forcing mechanisms for mid-Cretaceous black shale formation: evidence from the Upper Aptian and Lower Albian of the Vocontian Basin (SE France), Palaeogeography, Palaeoclimatology, Palaeoecology, 190, 710 399-426, https://doi.org/10.1016/S0031-0182(02)00616-8, 2003.

Hofmann, P., and Wagner, T.: ITCZ controls on Late Cretaceous black shale sedimentation in the tropical Atlantic Ocean, Paleoceanography and Paleoclimatology, 26, https://doi.org/10.1029/2011pa002154, 2011.

Huang, W.-Y., and Meinschein, W.: Sterols as ecological indicators, Geochim Cosmochim Ac, 43, 739-745, https://doi.org/10.1016/0016-7037(79)90257-6, 1979.

715 Izett, J. G., and Fennel, K.: Estimating the Cross-Shelf Export of Riverine Materials: Part 1. General Relationships From an Idealized Numerical Model, Global Biogeochemical Cycles, 32, 160-175, https://doi.org/10.1002/2017gb005667, 2018.

Jacquin, T., and De Graciansky, P. C.: Cyclic fluctuations of anoxia during Cretaceous time in the South Atlantic Ocean, Marine and petroleum geology, 5, 359-369, 1988.

Jenkyns, H. C.: Geochemistry of oceanic anoxic events, Geochemistry, Geophysics, Geosystems, 11, 1-30, 720 https://doi.org/10.1029/2009gc002788, 2010.

Jing, D., and Bainian, S.: Early Cretaceous atmospheric CO2 estimates based on stomatal index of Pseudofrenelopsis papillosa (Cheirolepidiaceae) from southeast China, Cretaceous Research, 85, 232-242, https://doi.org/10.1016/j.cretres.2017.08.011, 2018.

Kagami, H.: Sedimentary features of Cape Basin and Angola Basin sediments, DSDP Leg 40, Initial Reports of the Deep Sea Drilling Project, Volume 40, 40, 525, https://doi.org/10.2973/dsdp.proc.40.108.1978, 1978.

725 Kolonic, S., Wagner, T., Forster, A., Sinninghe Damsté, J. S., Walsworth-Bell, B., Erba, E., Turgeon, S., Brumsack, H. J., Chellai, E. H., and Tsikos, H.: Black shale deposition on the northwest African Shelf during the Cenomanian/Turonian oceanic anoxic event: Climate coupling and global organic carbon burial, Paleoceanography, 20, https://doi.org/10.1029/2003pa000950, 2005.

Koopmans, M. P., Köster, J., Van Kaam-Peters, H. M. E., Kenig, F., Schouten, S., Hartgers, W. A., de Leeuw, J. W., and Sinninghe Damsté, J. S.: Diagenetic and catagenetic products of isorenieratene: molecular indicators for photic zone anoxia, Geochim Cosmochim Ac, 60, 4467-730 4496, https://doi.org/10.1016/s0016-7037(96)00238-4, 1996.

Kounov, A., Viola, G., De Wit, M., and Andreoli, M.: A Mid Cretaceous paleo-Karoo River valley across the Knersvlakte plain (northwestern coast of South Africa): Evidence from apatite fission-track analysis, South African Journal of Geology, 111, 409-420, https://doi.org/10.2113/gssajg.111.4.409, 2008.

Lampitt, R., Salter, I., and Johns, D.: Radiolaria: Major exporters of organic carbon to the deep ocean, Global Biogeochemical Cycles, 23, 735 https://doi.org/10.1029/2008gb003221, 2009.

Laskar, J., Fienga, A., Gastineau, M., and Manche, H.: La2010: a new orbital solution for the long-term motion of the Earth, Astronomy & Astrophysics, 532, A89, https://doi.org/10.1051/0004-6361/201116836, 2011.

Leventhal, J. S.: An interpretation of carbon and sulfur relationships in Black Sea sediments as indicators of environments of deposition, Geochim Cosmochim Ac, 47, 133-137, https://doi.org/10.1016/0016-7037(83)90097-2, 1983.

740 Little, S. H., Vance, D., Lyons, T. W., and McManus, J.: Controls on trace metal authigenic enrichment in reducing sediments: insights from modern oxygen-deficient settings, American Journal of Science, 315, 77-119, https://doi.org/10.2475/02.2015.01, 2015.

Macdonald, D., Gomez-Perez, I., Franzese, J., Spalletti, L., Lawver, L., Gahagan, L., Dalziel, I., Thomas, C., Trewin, N., and Hole, M.: Mesozoic break-up of SW Gondwana: implications for regional hydrocarbon potential of the southern South Atlantic, Marine and Petroleum Geology, 20, 287-308, https://doi.org/10.1016/s0264-8172(03)00045-x, 2003.

745 Madec, G. V.: NEMO Ocean engine, Institut Pierre-Simon Laplace (IPSL), Paris (France), Note du Pôle de modélisation No 27, 2008.

Matthews, K. J., Maloney, K. T., Zahirovic, S., Williams, S. E., Seton, M., and Müller, R. D.: Global plate boundary evolution and kinematics since the late Paleozoic, Global and Planetary Change, 146, 226-250, https://doi.org/10.1016/j.gloplacha.2016.10.002, 2016.

McAnena, A., Flögel, S., Hofmann, P., Herrle, J. O., Griesand, A., Pross, J., Talbot, H. M., Rethemeyer, J., Wallmann, K., and Wagner, T.: Atlantic cooling associated with a marine biotic crisis during the mid-Cretaceous period, Nature Geoscience, 6, 558-561,
750 https://doi.org/10.1038/ngeo1850, 2013.

McLennan, S., Hemming, S., McDaniel, D., and Hanson, G.: Geochemical approaches to sedimentation, provenance, and tectonics, in: Processes Controlling the Composition of Clastic Sediments, edited by: Johnsson, M., and Basu, A., GSA Special Papers, 284, Geological Society of America, Boulder (USA), 21-40, https://doi.org/10.1130/spe284-p21, 1993.

Melguen, M.: Facies evolution, carbonate dissolution cycles in sediments from the eastern South Atlantic (DSDP Leg 40) since the Early
755 Cretaceous, in: Initial Reports of the Deep Sea Drilling Project, Volume 40, edited by: Bolli, H. M., and Ryan, W. B. F., U.S. Government Printing Office, Washington DC (USA), 981-1024, https://doi.org/10.2973/dsdp.proc.40.129.1978, 1978.

Menegatti, A. P., Weissert, H., Brown, R. S., Tyson, R. V., Farrimond, P., Strasser, A., and Caron, M.: High-resolution $\delta^{13}C$ stratigraphy through the early Aptian "Livello Selli" of the Alpine Tethys, Paleoceanography, 13, 530-545, https://doi.org/10.1029/98pa01793, 1998.

Meyer, K. M., and Kump, L. R.: Oceanic Euxinia in Earth History: Causes and Consequences, Annual Review of Earth and Planetary
760 Sciences, 36, 251-288, https://doi.org/10.1146/annurev.earth.36.031207.124256, 2008.

Moldowan, J. M., Seifert, W. K., and Gallegos, E. J.: Relationship between petroleum composition and depositional environment of petroleum source rocks, AAPG Bulletin, 69, 1255-1268, https://doi.org/10.1306/ad462bc8-16f7-11d7-8645000102c1865d, 1985.

Moldowan, J. M., Fago, F. J., Lee, C. Y., Jacobson, S. R., Watt, D. S., Slougui, N. E., Jeganathan, A., and Young, D. C.: Sedimentary 24-n-Propylcholestanes, Molecular Fossils Diagnostic of Marine Algae, Science, 247, 309-312, https://doi.org/10.1126/science.247.4940.309,
765 1990.

Moore, A., Blenkinsop, T., and Cotterill, F.: Southern African topography and erosion history: plumes or plate tectonics?, Terra Nova, 21, 310-315, https://doi.org/10.1111/j.1365-3121.2009.00887.x, 2009.

Naafs, B. D. A., and Pancost, R. D.: Environmental conditions in the South Atlantic (Angola Basin) during the Early Cretaceous, Org Geochem, 76, 184-193, https://doi.org/10.1016/j.orggeochem.2014.08.005, 2014.

770 Naafs, B. D. A., Castro, J. M., De Gea, G. A., Quijano, M. L., Schmidt, D. N., and Pancost, R. D.: Gradual and sustained carbon dioxide release during Aptian Oceanic Anoxic Event 1a, Nature Geoscience, 9, 135-139, https://doi.org/10.1038/ngeo2627, 2016.

Natland, J. H.: Composition, provenance, and diagenesis of Cretaceous clastic sediments drilled on the Atlantic continental rise off Southern Africa, DSDP Site 361; implications for the early circulation of the South Atlantic, in: Initial Reports of the Deep Sea Drilling Project, Volume 40, edited by: Bolli, H. M., and Ryan, W. B. F., U.S. Government Printing Office, Washington DC (USA), 1025-1061,
775 https://doi.org/10.2973/dsdp.proc.40.130.1978, 1978.

Nettersheim, B. J., Brocks, J. J., Schwelm, A., Hope, J. M., Not, F., Lomas, M., Schmidt, C., Schiebel, R., Nowack, E. C., and De Deckker, P.: Putative sponge biomarkers in unicellular Rhizaria question an early rise of animals, Nature Ecology & Evolution, 3, 577, https://doi.org/10.1038/s41559-019-0806-5, 2019.

780 O'Brien, C. L., Robinson, S. A., Pancost, R. D., Sinninghe Damsté, J. S., Schouten, S., Lunt, D. J., Alsenz, H., Bornemann, A., Bottini, C., and Brassell, S. C.: Cretaceous sea-surface temperature evolution: Constraints from TEX$_{86}$ and planktonic foraminiferal oxygen isotopes, Earth-Sci Rev, 172, 224-247, https://doi.org/10.1130/abs/2018am-323378, 2017.

Park, W., Keenlyside, N., Latif, M., Ströh, A., Redler, R., Roeckner, E., and Madec, G.: Tropical Pacific climate and its response to global warming in the Kiel Climate Model, Journal of Climate, 22, 71-92, https://doi.org/10.1175/2008jcli2261.1, 2009.

Partridge, T. C., and Maud, R. R.: Geomorphic evolution of southern Africa since the Mesozoic, South African Journal of Geology, 90, 179-
785 208, 1987.

Pedersen, T., and Calvert, S.: Anoxia vs. Productivity: What Controls the Formation of Organic-Carbon-Rich Sediments and Sedimentary Rocks?, AAPG Bulletin, 74, 454-466, https://doi.org/10.1306/0c9b232b-1710-11d7-8645000102c1865d, 1990.

Pérez-Díaz, L., and Eagles, G.: South Atlantic paleobathymetry since early Cretaceous, Scientific Reports, 7, 11819, https://doi.org/10.1038/s41598-017-11959-7, 2017.

790 Peters, K. E., Walters, C. C., and Moldowan, J. M.: The Biomarker Guide: Volume 2, Biomarkers and Isotopes in Petroleum Exploration and Earth History, Cambridge University Press, New York City, U.S.A., 1155 pp., 2007.

Proto Decima, F., Medizza, F., and Todesco, L.: Southeastern Atlantic Leg 40 calcareous nannofossils, in: Initial Reports of the Deep Sea Drilling Project, Volume 40, edited by: Bolli, H. M., and Ryan, W. B. F., 40, U.S. Government Printing Office, Washington DC (USA), 571-634, 1978.

795 Raiswell, R., Buckley, F., Berner, R. A., and Anderson, T. F.: Degree of pyritization of iron as a paleoenvironmental indicator of bottom-water oxygenation, Journal of Sedimentary Research, 58, 812-819, https://doi.org/10.1306/212f8e72-2b24-11d7-8648000102c1865d, 1988.

Ravnås, R., and Steel, R.: Architecture of marine rift-basin successions, AAPG Bulletin, 82, 110-146, https://doi.org/10.1306/1d9bc3a9-172d-11d7-8645000102c1865d, 1998.

Raynaud, J. F., and Robert, P.: Microscopical survey of organic matter from DSDP sites 361, 362, and 364, in: Initial reports of the Deep
800 Sea Drilling Project, Volume 40, edited by: Bolli, H. M., and Ryan, W. B. F., U.S. Government Printing Office, Washington DC (USA), 663-669, https://doi.org/10.2973/dsdp.proc.38394041s.306.1978, 1978.

Roeckner, E., Bäuml, G., Bonaventura, L., Brokopf, R., Esch, M., Giorgetta, M., Hagemann, S., Kirchner, I., Kornblueh, L., Manzini, E., Rhodin, A., Schlese, U., Schulzweida, A., and Tompkins, A.: The atmospheric general circulation model ECHAM 5. PART I: Model description, Max Planck Institute for Meteorology, Hamburg (Germany), Report No. 349, 2003.

805 Schlanger, S. O., and Jenkyns, H. C.: Cretaceous oceanic anoxic events: causes and consequences, Geologie en Mijnbouw, 55, 179-184, 1976.

Sewall, J. O., van de Wal, R. S. W., van der Zwan, K., van Oosterhout, C., Dijkstra, H. A., and Scotese, C. R.: Climate model boundary conditions for four Cretaceous time slices, Clim Past, 3, 647-657, https://doi.org/10.5194/cpd-3-791-2007, 2007.

Sharples, J., Middelburg, J. J., Fennel, K., and Jickells, T. D.: What proportion of riverine nutrients reaches the open ocean?, Global
810 Biogeochemical Cycles, 31, 39-58, https://doi.org/10.1002/2016gb005483, 2017.

Sinninghe Damsté, J. S., Kuypers, M. M. M., Schouten, S., Schulte, S., and Rullkötter, J.: The lycopane/C31 n-alkane ratio as a proxy to assess palaeoxicity during sediment deposition, Earth Planet Sc Lett, 209, 215-226, https://doi.org/10.1016/s0012-821x(03)00066-9, 2003.

Stein, R., Rullkötter, J., and Welte, D. H.: Accumulation of organic-carbon-rich sediments in the Late Jurassic and Cretaceous Atlantic Ocean—A synthesis, Chemical Geology, 56, 1-32, https://doi.org/10.1016/0009-2541(86)90107-5, 1986.

815   Steinig, S., Dummann, W., Park, W., Latif, M., Kusch, S., Hofmann, P., and Flögel, S.: Evidence for a regional warm bias in the Early Cretaceous TEX86 record, Earth Planet Sc Lett, 539, 116184, https://doi.org/10.1016/j.epsl.2020.116184, 2020.

The Shipboard Scientific Party, S.: Cape Basin continental rise; Sites 360 and 361, in: Initial Reports of the Deep Sea Drilling Project, Volume 40, edited by: Bolli, H. M., and Ryan, W. B. F., U.S. Government Printing Office, Washington DC (USA), 29-182, https://doi.org/10.2973/dsdp.proc.40.102.1978, 1978.

820   Thiede, J., and Van Andel, T. H.: The paleoenvironment of anaerobic sediments in the late Mesozoic South Atlantic Ocean, Earth Planet Sc Lett, 33, 301-309, https://doi.org/10.1016/0012-821x(77)90082-6, 1977.

Trabucho Alexandre, J., Hay, W. W., and de Boer, P. L.: Phanerozoic environments of black shale deposition and the Wilson Cycle, Solid Earth, 3, 29-42, https://doi.org/10.5194/se-3-29-2012, 2012.

Tribovillard, N., Algeo, T. J., Lyons, T., and Riboulleau, A.: Trace metals as paleoredox and paleoproductivity proxies: an update, Chemical
825   Geology, 232, 12-32, https://doi.org/10.1016/j.chemgeo.2006.02.012, 2006.

Twining, B. S., Baines, S. B., Vogt, S., and Nelson, D. M.: Role of diatoms in nickel biogeochemistry in the ocean, Global Biogeochemical Cycles, 26, GB4001, https://doi.org/10.1029/2011gb004233, 2012.

Tyson, R.: The "productivity versus preservation" controversy: cause, flaws, and resolution, in: The Deposition of Organic-Carbon-Rich Sediments: Models, Mechanisms, and Consequences, edited by: Harris, N., SEPM Special Publication, 82, SEPM Society for Sedimentary
830   Geology, Tulsa (USA), 17-33, https://doi.org/10.2110/pec.05.82.0017, 2005.

Van Andel, T. H., Thiede, J., Sclater, J. G., and Hay, W. W.: Depositional history of the South Atlantic Ocean during the last 125 million years, The Journal of Geology, 85, 651-698, https://doi.org/10.1086/628357, 1977.

Wagner, T., and Pletsch, T.: Tectono-sedimentary controls on Cretaceous black shale deposition along the opening Equatorial Atlantic Gateway (ODP Leg 159), in: The Oil and Gas Habitats of the South Atlantic, edited by: Cameron, N. R., Bate, R. H., and Clure, V. S.,
835   Special Publications, 153, Geological Society of London, London (UK), 241-265, https://doi.org/10.1144/GSL.SP.1999.153.01.15, 1999.

Wagner, T., Hofmann, P., and Flögel, S.: Marine black shale deposition and Hadley Cell dynamics: A conceptual framework for the Cretaceous Atlantic Ocean, Marine and Petroleum Geology, 43, 222-238, https://doi.org/10.1016/j.marpetgeo.2013.02.005, 2013.

Wanty, R. B., and Goldhaber, M. B.: Thermodynamics and kinetics of reactions involving vanadium in natural systems: Accumulation of vanadium in sedimentary rocks, Geochim Cosmochim Ac, 56, 1471-1483, https://doi.org/10.1016/0016-7037(92)90217-7, 1992.

840   Weaver, C. E., and Pollard, L. D.: The Chemistry of Clay Minerals, Developments in Sedimentology, 15, Elsevier, Amsterdam (Netherlands), 212 pp., 1973.

Wedepohl, K. H.: Environmental influences on the chemical composition of shales and clays, Physics and Chemistry of the Earth, 8, 307-333, https://doi.org/10.1016/0079-1946(71)90020-6, 1971.

Wedepohl, K. H.: The Composition of Earth's Upper Crust, Natural Cycles of Elements, Natural Resources, in: Metals and Their Compounds
845   in the Environment, edited by: Merian, E., Anke, M., Ihnat, M., and Stoeppler, M., Wiley-VCH, Weinheim (Germany), 3-17, 2004.

Weissert, H., Lini, A., Föllmi, K. B., and Kuhn, O.: Correlation of Early Cretaceous carbon isotope stratigraphy and platform drowning events: a possible link?, Palaeogeography, Palaeoclimatology, Palaeoecology, 137, 189-203, https://doi.org/10.1016/S0031-0182(97)00109-0, 1998.

850 Zimmerman, H. B., Boersma, A., and McCoy, F. W.: Carbonaceous sediments and palaeoenvironment of the Cretaceous South Atlantic Ocean, in: Marine Petroleum Source Rocks, edited by: Brooks, J., and Fleet, A. J., Special Publications, 26, Geological Society of London, Oxford (UK), 271-286, https://doi.org/10.1144/gsl.sp.1987.026.01.19, 1987.
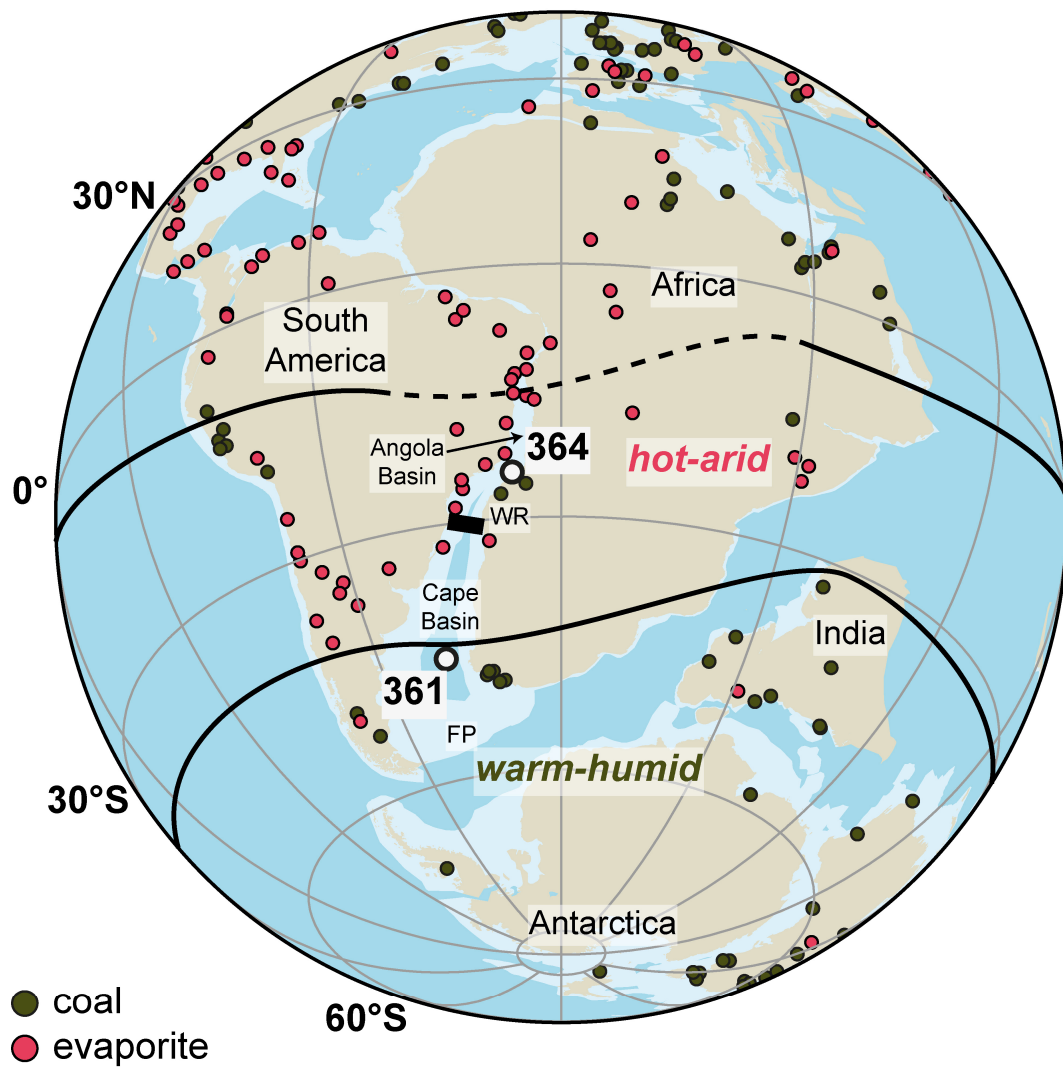
855

Figure 1: Aptian paleogeographic reconstruction (Matthews et al., 2016) showing the Early Cretaceous distribution of climate sensitive rock types (Boucot et al., 2013; Cao et al., 2019). Position of climate belts according to Boucot et al. (2013) and Chumakov et al. (1995). Land–sea mask and distribution of shelf seas were adapted from Cao et al. (2017). WR: Walvis Ridge, FP: Falkland
860 **Plateau.**
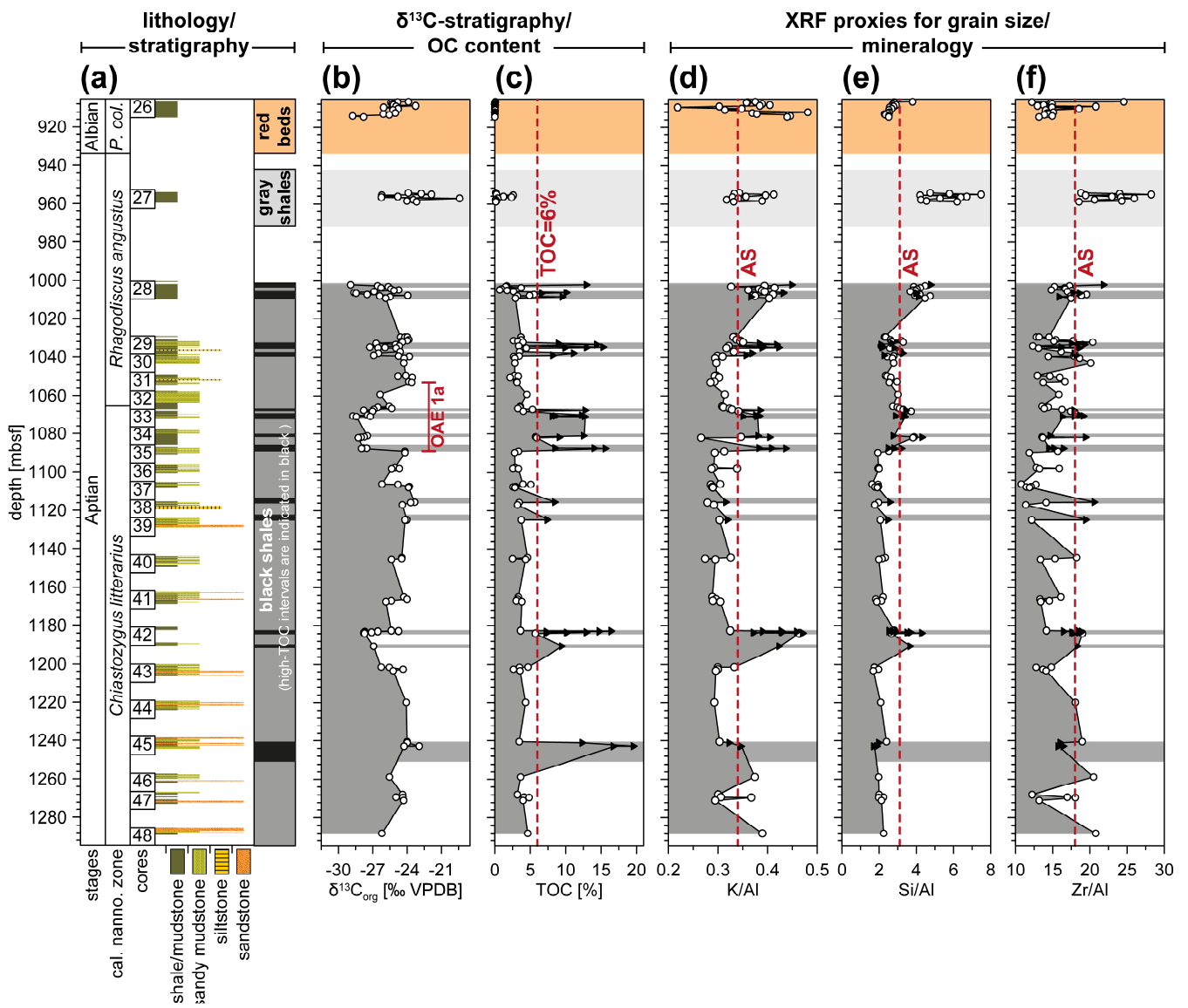
Figure 2: Stratigraphic framework and inorganic geochemistry at DSDP Site 361: (a) stage assignment, calcareous nannofossil zonation, and lithology of the studied sediment sequence, (b) bulk δ13Corg, (c) total organic carbon content, (d) K/Al ratios, (e) Si/Al ratios, and (f) Zr/Al ratios. Black triangles with background shading indicate high-TOC black shales (>6% TOC). Dashed lines in (d)–(f) represent average shale (AS) ratios. Bulk δ13Corg data and TOC content are taken from Dummann et al. (2020). *P. col.* = *Prediscosphaera columnata*

865
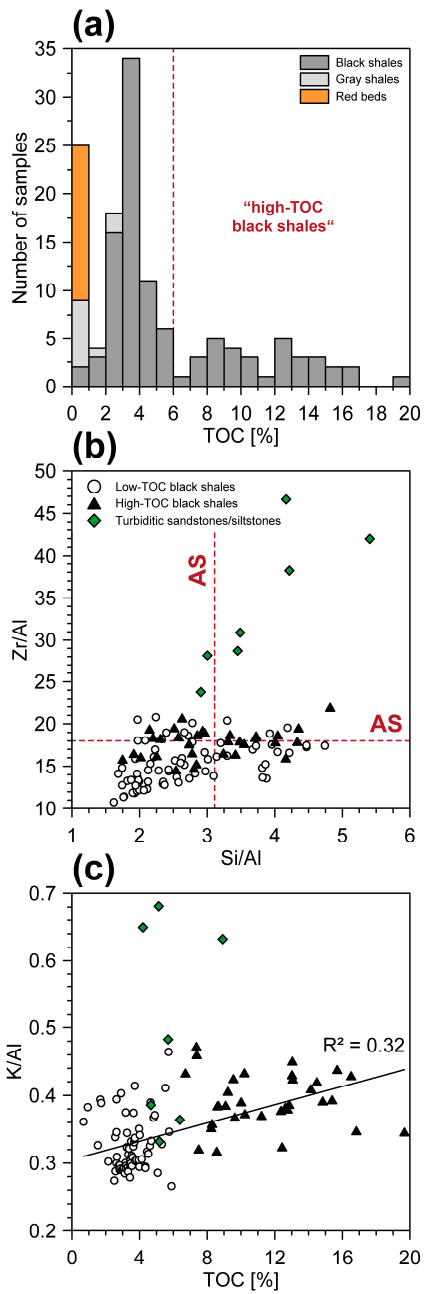
870 **Figure 3: Geochemical characteristics of the different lithostratigraphic (sub-)units: (a) histogram showing the TOC contents of samples from different lithostratigraphic units (i.e. black shales, gray shales, and red beds). Panel (b) shows cross-plots of XRF-derived grain-size proxies Si/Al and Zr/Al for black shale samples, which are grouped into high-TOC black shales (TOC>6 %) and low-TOC black shales (TOC<6 %). Green diamonds represent samples taken from intercalated sandstones, which are plotted for reference. Panel (c) shows cross-plots of TOC content and K/Al ratios. AS: average shale**
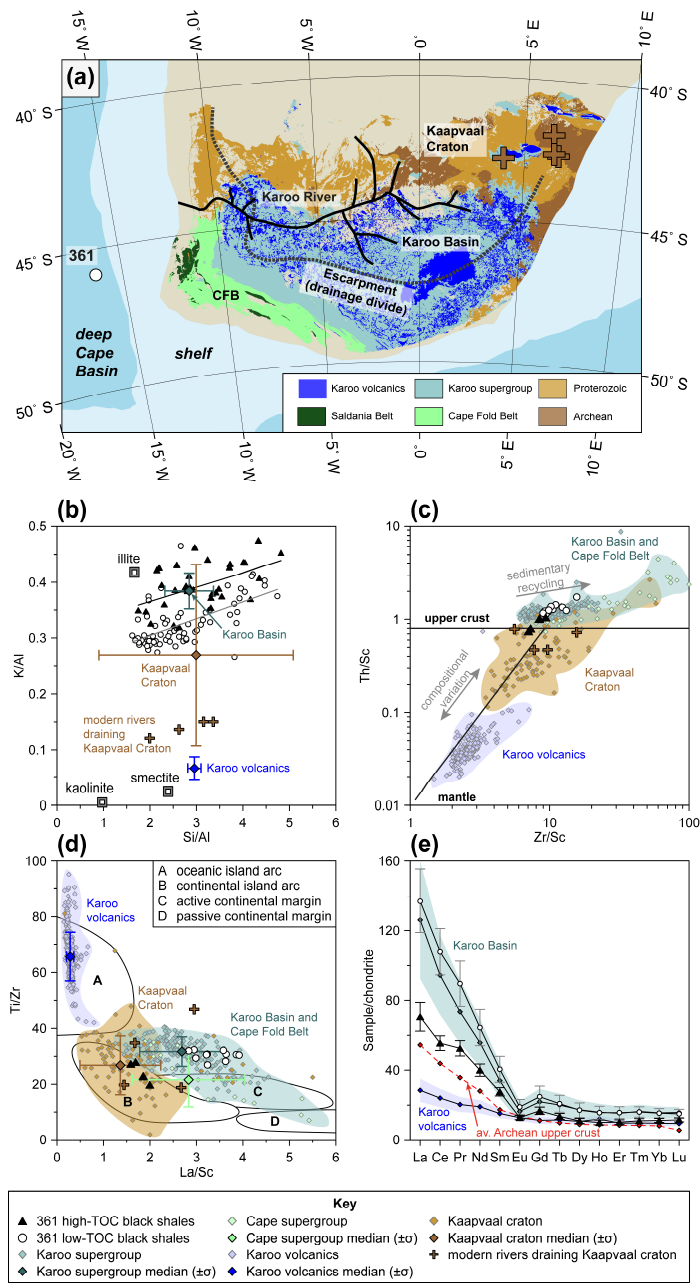
Figure 4: Provenance assessment of Early Aptian black shales based on major and trace metal discrimination plots: (a) geological map of South Africa showing potential sediment source areas. Early Cretaceous paleo-drainage reconstruction was adapted from De Wit (1999). Panel (b) shows cross-plots of Si/Al and K/Al. Average elemental composition of different clay minerals was taken from Weaver and Pollard (1973). Panels (c) and (d) show cross-plots of Zr/Sc vs. Th/Sc (McLennan et al., 1993) and La/Sc vs. Ti/Zr (Bhatia and Crook, 1986), respectively. Panel (e) shows chondrite-normalized rare earth element distributions. Trace element data for source areas were compiled from the literature. Data and references are provided in Supplements S2 and S3.
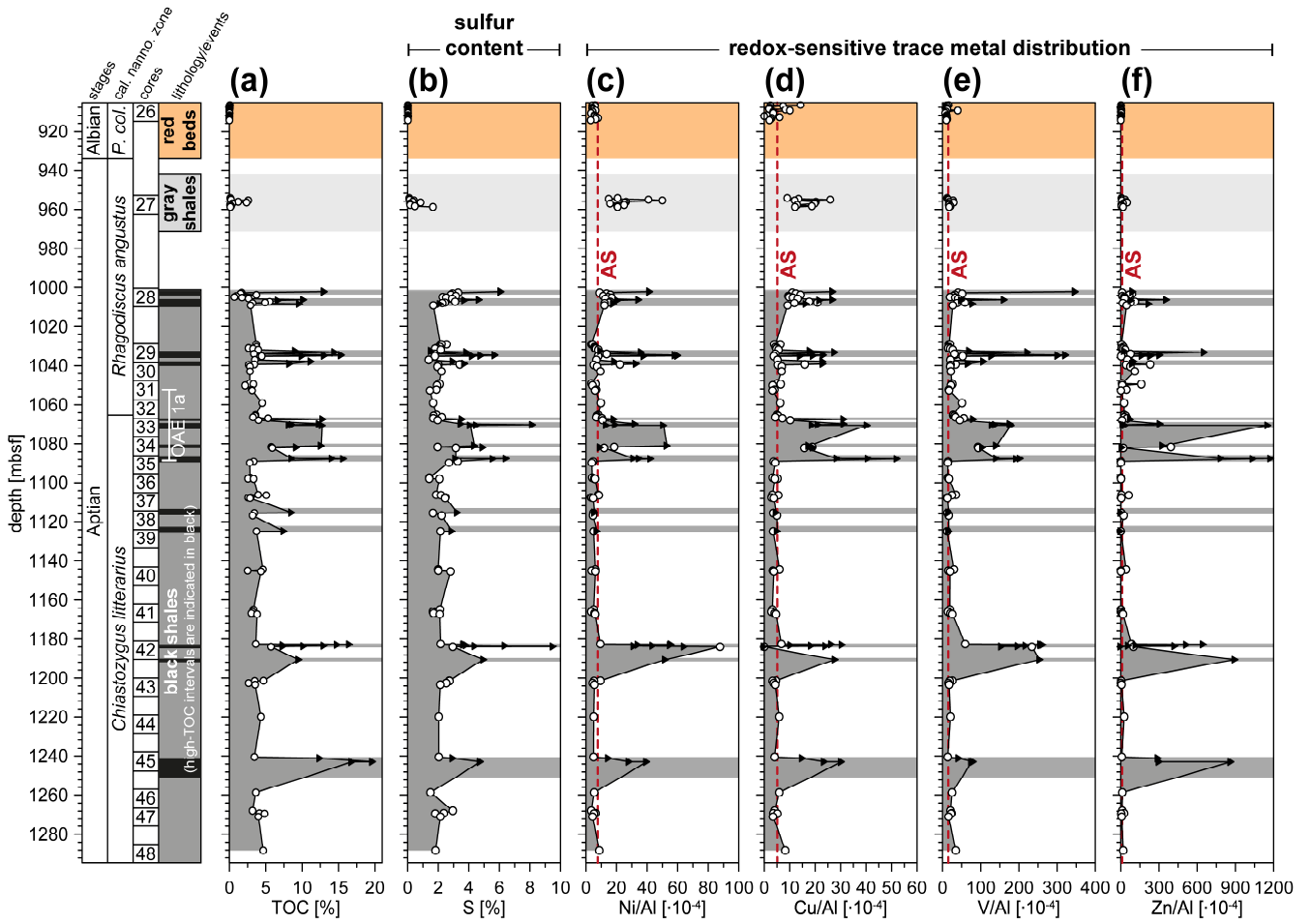
Figure 5: Inorganic geochemical parameters used to reconstruct paleo-redox conditions: (a) total organic carbon content (Dummann et al., 2020), (b) total sulfur content, (c)–(f): Ni/Al, Cu/Al, V/Al, and Zn/Al ratios. Black triangles with background shading indicate high-TOC black shales (>6% TOC). Average shale TM/Al ratios (AS) are plotted as red dashed lines. *P. col.* = *Prediscosphaera columnata*

885

890
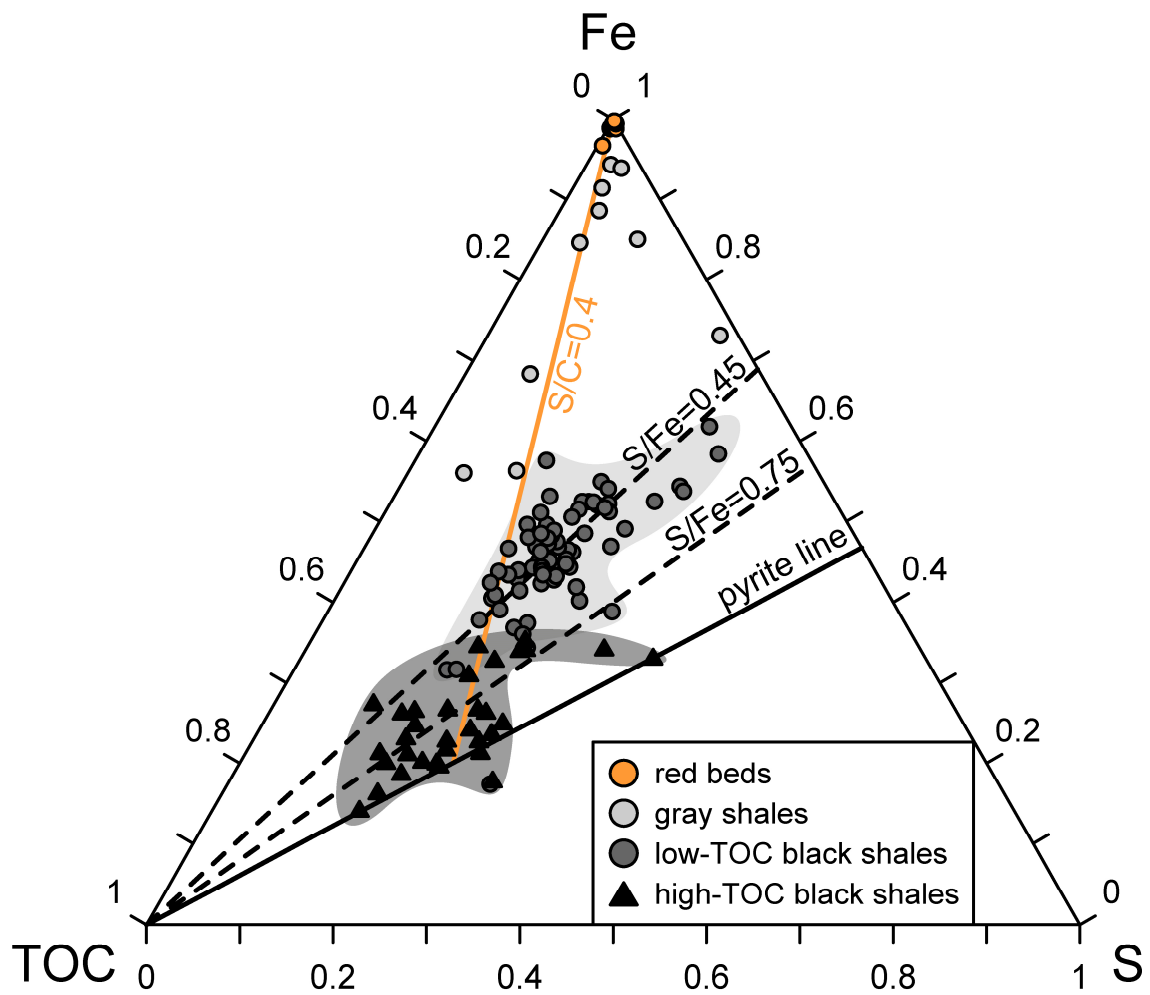
Figure 6: Ternary diagram illustrating TOC-S-Fe relationships in the different lithostratigraphic (sub-)units. Characteristic S/Fe and S/C ratios used to discriminate redox states (i.e. oxic conditions: S/C=0.4 and S/Fe<0.45, suboxic–anoxic conditions: S/Fe=0.45–0.75, and strictly anoxic–euxinic conditions: S/Fe>0.75) are plotted as proposed by Raiswell et al. (1988), Leventhal (1983) and Berner and Raiswell (1983). TOC data are taken from Dummann et al. (2020).

895
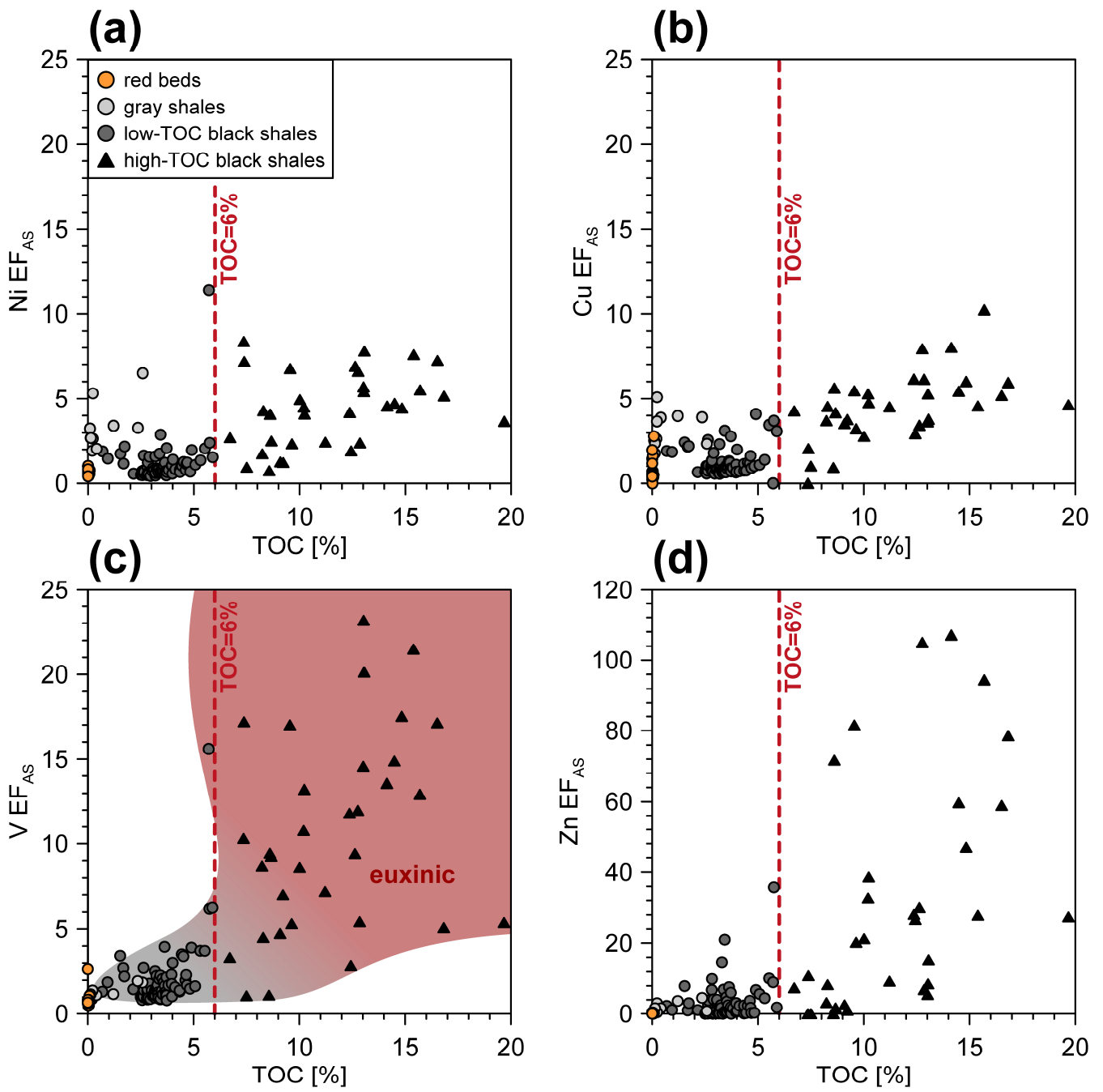
Figure 7: Cross-plots of total organic carbon content and average shale-normalized enrichment factors (EF$_{AS}$) of (a) Ni, (b) Cu, (c) V, (d) Zn. Black triangles indicate high-TOC black shales (>6% TOC). TOC data are taken from Dummann et al. (2020).
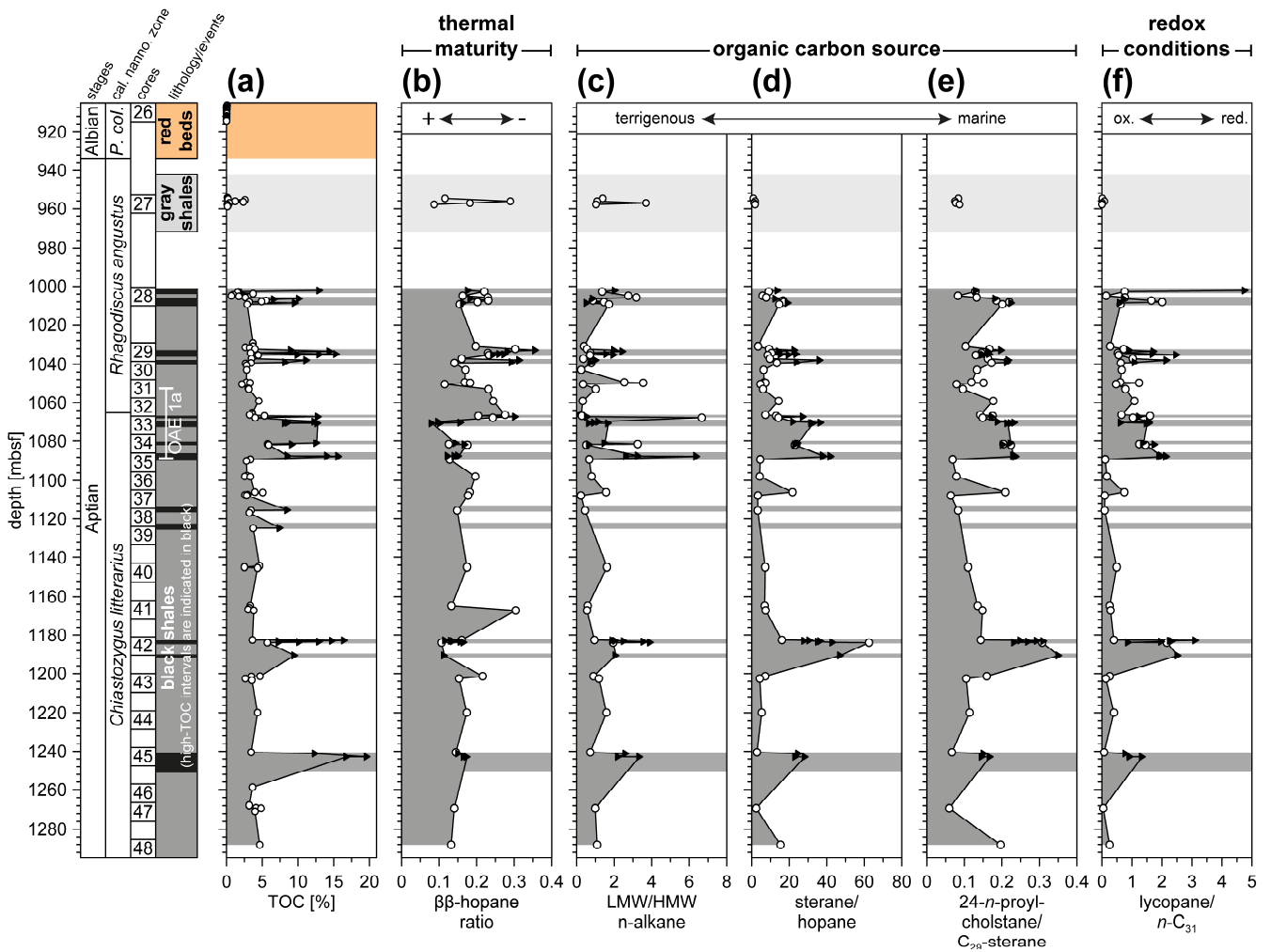
Figure 8: Distribution of selected biomarker parameters used to reconstruct thermal maturity, OC source, and paleo-redox conditions: (a) total organic carbon content (Dummann et al., 2020), (b) $\beta\beta/(\beta\beta+\alpha\beta+\beta\alpha)$-$C_{30}$-hopane ratio, (c) low molecular weight/high molecular weight *n*-alkane ratio, (d) sterane/hopane ratio, (e) 24-*n*-propylcholestane/C_{29}-sterane ratio, and (f) lycopane/*n*-C_{31} ratio. Black triangles with background shading indicate high-TOC black shales (>6% TOC). *P. col.* = *Prediscosphaera columnata*
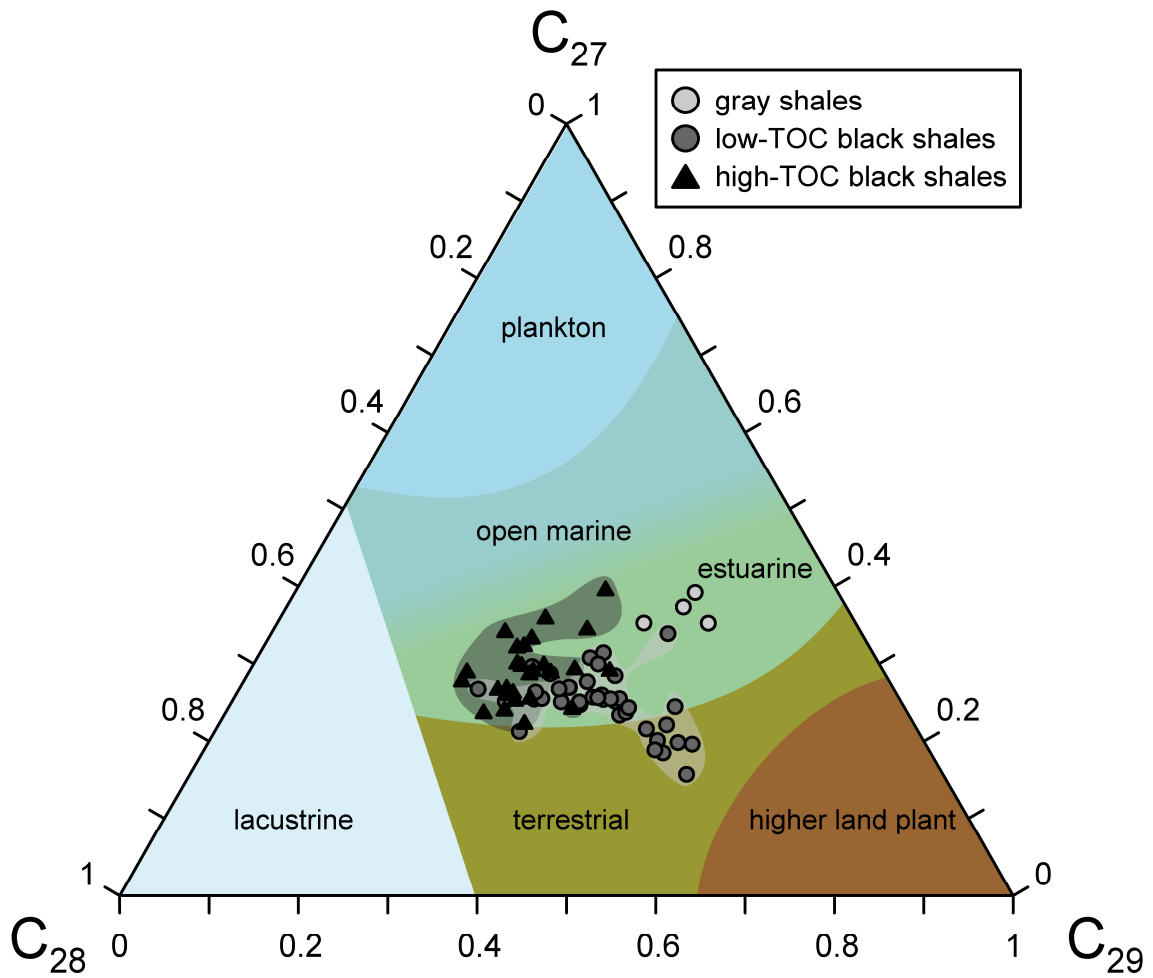
910

Figure 9: Ternary diagram showing the distribution of regular desmethylsteranes in gray shales, low-TOC black shales (<6% TOC), and high-TOC black shales (>6% TOC). Organic carbon source end-members were adapted from Huang and Meinschein (1979).
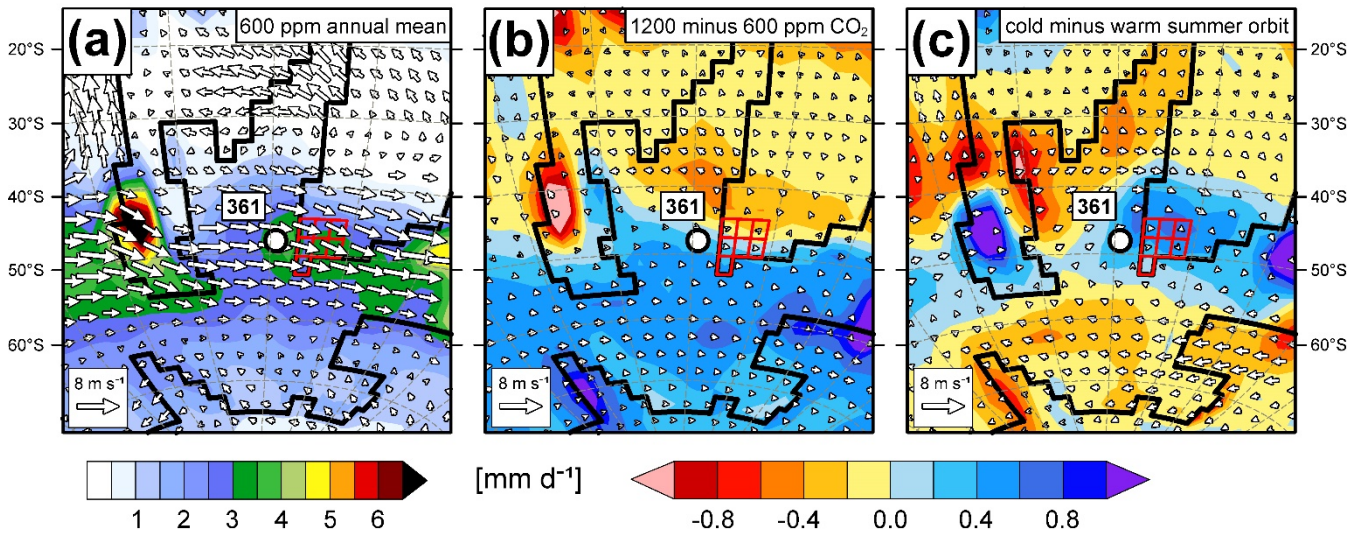
Figure 10: Large-scale atmospheric circulation and climate sensitivity of the study region: (a) simulated annual mean surface wind and precipitation at 600 ppm $p\text{CO}_2$ and modern orbital configuration, (b) mean annual wind and precipitation changes due to a doubling of atmospheric $p\text{CO}_2$ (constant orbital configuration), and (c) mean annual wind and precipitation changes related to orbital forcing (i.e. difference between cold and warm summer orbital configuration at 600 ppm $p\text{CO}_2$). Highlighted grid points show proposed catchment area. For more details on the modeling data the reader is referred to Supplement S4.
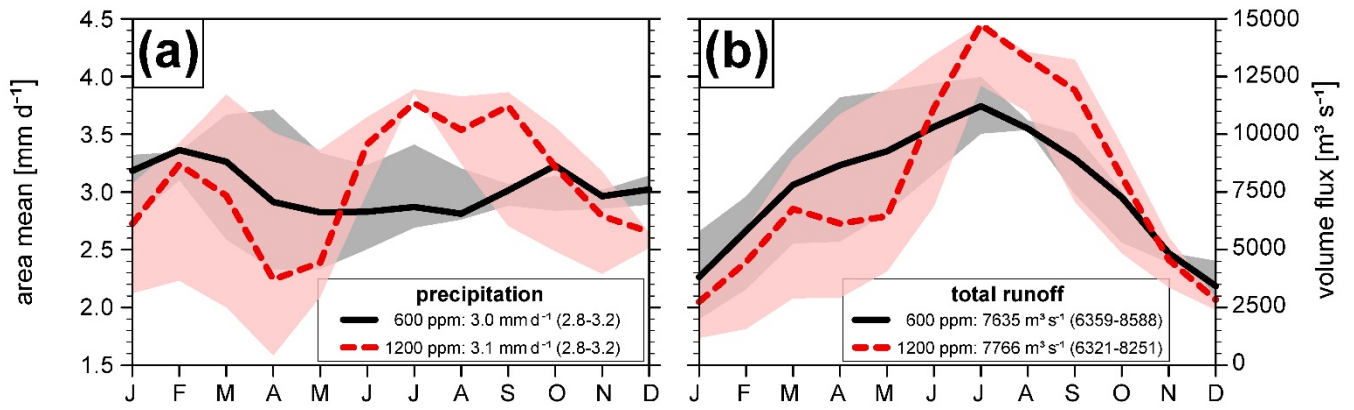
Figure 11: Annual cycle of (a) simulated precipitation and (b) total run-off averaged or integrated over the ~450.000 km² large catchment area shown in Figure 10. Solid and dashed lines show simulations using a modern orbital configuration at 600 and 1200 ppm pCO₂, respectively. Red and grey shadings represent precipitation and run-off ranges related to changes in orbital configuration at 600 and 1200 ppm pCO₂, respectively. Annual means for modern orbit simulations are provided in legends. Results for the "cold summer orbit" (i.e. maximum precipitation and run-off) and "warm summer orbit" (i.e. minimum precipitation and run-off) simulations are listed in parentheses.